Supporting Information

1. Experimental Section

***Materials*:** PM6 and D18-Cl were purchased from Organtec. Ltd. PNDIT-F3N was purchased from eFlex PV. PY-SSe and PY-Cl were synthesized by our group according to the literature. Chloroform was distilled from CaH_2 prior to use. Other reagents used were purchased from commercial sources and used as received.

***Contact angle measurements and surface energy calculation*:** The contact angles of two polymer acceptors (PY-SSe and PY-Cl) and two polymer donors (PM6 and D18-Cl) were measured using a Contact Angle Analyzer. The contact angles of two different solvents (water and ethylene glycol (EG)) on the neat films were used to calculate the surface tension of each film.

***Surface Energy and Flory-Huggins' χ parameter*:** The surface energy of the relevant pristine and blend films is calculated using the Owens two-liquid method, in which water and ethylene glycol were chosen as polar and nonpolar solvents, respectively.

$$\gamma_L(1 + cos\theta) = 2\left(\gamma_S^d\gamma_L^d\right)^{1/2} + 2\left(\gamma_S^p\gamma_L^p\right)^{1/2}$$

Here, γ_L^d and γ_L^p are the dispersive and polar components of the liquid used to calculate the surface energy, and $\gamma_L = \gamma_L^d + \gamma_L^p$ is the total surface energy, θ is the contact angle of the droplet. Based on a system of binary equations consisting of equations listed from two sets of contact angle data, we can solve for the dispersion (γ_S^d) and polarity (γ_S^p) components of the surface energy of the film.

The Flory-Huggins interaction parameter χ_{D-A} is derived using the empirical equation: $\chi_{D-A} = K(\sqrt{\gamma_D} - \sqrt{\gamma_A})^2$, where K is a positive constant; γ_D and γ_A are surface energy values. Here we follow the tradition of taking the value of K as 1 for the convenience of calculation. [1-3]

***Conventional device fabrication and testing*:** Solar cell devices fabrication: The solar cell devices were fabricated with a structure of Glass/ITO/PEDOT: PSS (20 nm, purchased from Xi'an Yuri Solar Co., Ltd. Corp 4083)/Active layer/PNDIT-F3N/Ag. Pre-patterned ITO-coated glass substrates (purchased from South China Science & Technology Company Limited, the sheet resistance of the ITO glass was about 15 ohms per square) washed with methylbenzene, deionized water, acetone, and isopropyl alcohol in an ultrasonic bath for 15 minutes each. After blow-drying with high-purity nitrogen, all the cleaned ITO glass is next placed in the UV-Ozone cleaning instrument using ultraviolet ozone light irradiation for 15 minutes to obtain the UV-Ozone treated ITO anode. Subsequently, a thin layer of PEDOT: PSS was deposited through spin-coating at 4,000 rpm for the 30s on the pre-cleaned ITO-coated glass from a PEDOT: PSS aqueous solution and then annealed at 150 °C for 15 min in air. For the PM6:PY-SSe-based devices, the PM6:PY-SSe solution (1:1.2 by weight and total concentration of 10 mg/mL in chloroform with 1% of 1-chloronaphthalene additive by volume) was blade coated on the ITO/PEDOT:PSS substrates at different speed and then the substrates were put onto a hot plate and annealed at 100 ^{o}C for 5 mins. For the D18-Cl:PY-Cl based devices, the D18-Cl:PY-Cl solution (1:1.2 by weight and total concentration of 8 mg/mL in chloroform with 1% of 1-chloronaphthalene additive by volume and stirred at 50 ^{o}C for 2 hours) was blade coated on the ITO/PEDOT:PSS substrates at different speed and then the substrates were put onto a hot plate and annealed at 100 ^{o}C for 5 mins. For the Q-BHJ blend films, the PM6:PY-SSe solution (1:1.2 by weight and total concentration of 10 mg/mL in chloroform with 1% of 1-chloronaphthalene additive by volume) and D18-Cl:PY-Cl solution (1:1.2 by weight and total concentration of 8 mg/mL in chloroform with 1% of 1-chloronaphthalene additive by volume and stirred at 50 ^{o}C for 2 hours) were mixed at a volume ratio of 1:1 before deposition. The resultant mixed solution was kept at 50 ℃ before blade coated on the ITO/PEDOT:PSS substrates. The substrates were put onto a hot plate and annealed at 100 ℃ for 5 min. For the Q-LbL blend films, D18-Cl:PY-Cl solution (1:1.2 by weight and total concentration of 5 mg/mL in chloroform with 1% of 1-chloronaphthalene additive by volume and stirred at 50 ^{o}C for 2 hours) and PM6:PY-SSe solution (1:1.2 by weight and total concentration of 6 mg/mL in chloroform with 1% of 1-chloronaphthalene additive by volume) were sequentially blade coated on the ITO/PEDOT:PSS substrates and then were put onto a hot plate and annealed at 100 ^{o}C for 5 mins. The temperature of the base plate is set to 40 ^{o}C during all blade-coating processes. The thickness optimal active layer is measured by a Bruker Dektak XT stylus profilometer. A PNDIT-F3N layer via a solution concentration of 1 mg mL^{-1} in methanol with 5 v% of acetic acid was deposited at the top of the active layer at a rate of 4000 rpm for 30 s. Finally, the top argentum electrode of 100 nm thickness was thermally evaporated (Suzhou Fangsheng FS-300) through a mask onto the cathode buffer layer under a vacuum of～5×10^{-6} mbar. The typical active area of the investigated devices was 0.048 cm^2 and the area of a non-refractive mask used was 0.0289 cm^2. The current-voltage characteristics of the solar cells were measured by a Keithley 2400 source meter unit under AM 1.5G (100 mW cm^{-2}) irradiation from a solar simulator (Enlitech model SS-X160R). Solar simulator illumination intensity was determined at 100 mW cm^{-2} using a monocrystalline silicon reference cell with a KG5 filter. Short circuit currents under AM 1.5G (100 mW cm^{-2}) conditions were estimated from the spectral response and convolution with the solar spectrum. The forward scan was adopted to test the *J-V* curves, the scan step is 0.02 V and the delay time is 1 ms. The scan mode is sweep. The external quantum efficiency was measured by a Solar Cell Spectral Response Measurement System QE-R3011 (Enli Technology Co., Ltd.). For the device fabrication using halogen-free solvents, all active layer solutions are formulated the same as the CF solvents described above, and the materials were dissolved in the corresponding halogen-free solvent (i.e., toluene, tetrahydrofuran, and ortho-xylene) by stirring for 3 hours at 80 °C. During all blade-coating processes, the temperature of the base plate is set to 60 °C. Note that other device preparation conditions are the same as the above discussion on CF-based devices.

***Optical measurements*:** Ultraviolet-visible near-infrared (UV-vis-NIR) absorption spectra were recorded with a Perkin-Elmer Lambda 365 UV-Vis spectrophotometer from 300 nm to 1100 nm.

***Electrochemical measurement*:** Electrochemical measurements were carried out at room temperature in an acetonitrile solution of 0.1 mol L^{-1} Bu_4NPF_6 using ferrocene (-4.8 eV) as standard reference, with a computer-controlled CHI660C electrochemical workstation. All cyclic voltammetry (CV) curves were measured by films cast from $CHCl_3$ solution on the glassy carbon electrode with Pt wire as the counter electrode and Ag/AgCl as the reference electrode.

Time-of-Flight Secondary Ion Mass Spectrometry (TOF-SIMS) measurements: SIMS experiments were conducted using a TOF-SIMS (Tescan AMBER) instrument equipped with a Ga^+ liquid metal ion gun, Cesium sputtering gun, and electron flood gun for charge compensation. Ga^+ was used as the sputter source with a 2000 V energy and 1 nA current. The typical sputter area was $30 \times 30\ \mu m^2$.

***Space charge limited current (SCLC) measurement*:** Single carrier devices were fabricated and the dark current-voltage characteristics were measured and analyzed in the space charge limited (SCL) regime following the references. The single carrier devices were fabricated (the structure Glass/ITO/PEDOT:PSS/Active layer/MoO_3 (10nm)/Ag (100 nm) for hole-only devices and the structure was Glass/ITO/ZnO/Active layer/PNDIT-F3N/Ag for the electron only devices) and the dark current-voltage characteristics measured and analyzed in the space charge limited (SCL) regime. The *J-V* characteristics of both hole-only and electron-only diodes can be excellently fit by the Mott-Gurney law, which can be expressed as the following equation:

$$J = \frac{9}{8}\varepsilon_0\varepsilon_r\mu\frac{V^2}{L^3}exp\left(\frac{0.89\beta}{\sqrt{L}}\sqrt{V}\right) \quad (1)$$

Where *J* is current density, μ is the carrier mobility, $\varepsilon_0\varepsilon_r$ is the dielectric permittivity, *L* is the thickness of the active layer of corresponding devices and the β is the field activation factor. $V = V_{appl} - V_{bi}$, V_{appl} is the applied potential, and V_{bi} is the built-in potential which results from the difference in the work function of the anode and the cathode (in this device structure, $V_{bi} = 0.2$ V).

***Transient photocurrent (TPC) measurement*:** Relevant control and MSM solar cells were excited with a 405 nm laser diode. The transient photocurrent response of the devices at a short circuit condition to a 200 μs square pulse from the LED with no background illumination. The current traces were recorded on a Tektronix DPO3034 digital oscilloscope by measuring the voltage drop over a 5-ohm sensor resistor in series with the solar cell. DC voltage was applied to the solar cell with an MRF544 bipolar junction transistor in a common collector amplifier configuration.

***Transient photovoltage (TPV) measurement*:** In the TPV measurements, a 405 nm laser diode was used to keep the organic solar cells in open circuit conditions. Measuring the light intensity with a highly linear photodiode and driving the laser intensity with a waveform generator (Agilent 33500B) at one sun. Moreover, a small perturbation was induced with a second 405 nm laser diode. The intensity of the short laser pulse was adjusted to keep the voltage perturbation below 10 mV. After the pulse, the voltage decays back to its steady state value in a single exponential decay.

***FTPS-EQE spectra measurement*:** The FTPS measurements were recorded using a Bruker Vertex 70 Fourier-transform infrared (FTIR) spectrometer, equipped with a quartz tungsten halogen lamp, a quartz beam-splitter, and an external detector option. A low noise current amplifier (Femto DLPCA-200) was used to amplify the photocurrent produced on the illumination of the photovoltaic devices with light modulated by the FTIR. The output voltage of the current amplifier was fed back into the external detector port of the FTIR. The photocurrent spectrum was collected by FTIR's software.

***Urbach energy measurement*:** The energetic disorder can be quantized by a parameter of Urbach energy (E_U), which follows the Urbach rule expressed as follows:

$$\alpha(E) = \alpha_0 e^{\frac{(E - E_0)}{E_U}}$$

Here, $\alpha(E)$ is the absorption coefficient, α_0 and E_0 are two constants, and E is the photon energy. Smaller E_U represents lower energetic disorder. By fitting the FTPS-EQE curves with the above equation, the E_U values can be obtained.

***Electroluminescence Measurement*:** The EL signature was collected with a monochromator and detected with an InGaAs detector. The data collection range is 700 nm-1300 nm.

Bandgap of the devices: Bandgap is calculated from the following equation:

$$E_g = \frac{\int_a^b E_g \cdot P(E_g) \cdot dE_g}{\int_a^b P(E_g) \cdot dE_g}$$

Here, $P(E) = dEQE(E)/dE$ is obtained from the first-order derivative of EQE, and the integral boundaries a and b are selected at $P(a) = P(b) = 0.5 \times max[P(E_g)]$.

Energy loss analysis**:** The overall energy loss can be divided into three parts:

$$E_{loss} = E_g - qV_{OC} = \left(E_g - qV_{OC}^{SQ}\right) + \left(qV_{OC}^{SQ} - qV_{oc}^{rad}\right) + \left(qV_{oc}^{rad} - qV_{OC}\right)$$

$$= \left(E_g - qV_{OC}^{SQ}\right) + q\Delta V_{oc}^{rad,\,below\ gap} + q\Delta V_{oc}^{non-rad} = \Delta E_1 + \Delta E_2 + \Delta E_3$$

Where q is the elementary charge; V_{OC}^{SQ} is the maximum voltage given by the Shockley-Queisser limit; V_{oc}^{rad} is the open-circuit voltage when radiative recombination is the only recombination mechanism in the device; $\Delta V_{OC}^{rad,\,below\ gap}$ (ΔE_2) is the voltage loss of radiative recombination below the bandgap; $\Delta V_{OC}^{non-rad}$ (ΔE_3) is the voltage loss due to non-radiative recombination. The photovotlaic bandgap energy (E_{gap}) obtained from the. The detailed calculating methods of energy loss are as follows. The V_{oc} for any type of solar cell is determined by this formula:

$$V_{OC} = \frac{kT}{q}\ln\left(\frac{J_{SC}}{J_0} + 1\right)$$

Where k is the Boltzmann constant, T is the temperature, and q is the elementary charge. The expression of short-circuit current density (J_{SC}) and dark current density (J_0) are given by:

$$J_{sc} = q\int_0^\infty EQE_{PV}(E)\emptyset_{AM1.5G}(E)dE$$

$$J_0 = \frac{q}{EQE_{EL}}\int_{E_g}^\infty EQE_{PV}(E)\emptyset_{BB}(E)dE$$

Where EQE_{EL} is the radiative quantum efficiency of the solar cell with injected currents in dark condition.

When there is only radiative recombination in the device, EQE_{EL}= 1. In Shockley-Queisser limit theory, the external quantum efficiency is assumed to follow the form of the Heaviside function:

$$EQE_{PV}^{SQ}(E) = \begin{cases} 0, \ E < E_g \\ 1, \ E \geq E_g \end{cases}$$

Accordingly, the V_{oc}^{SQ} can be calculated by the equation:

$$V_{OC}^{SQ} = \frac{kT}{q}\ln\left(\frac{J_{SC}}{J_0} + 1\right) = \frac{kT}{q}\ln\left(\frac{q\int_0^\infty EQE_{PV}(E)\emptyset_{AM1.5G}(E)dE}{q\int_{E_g}^\infty \emptyset_{BB}(E)dE} + 1\right)$$

Likewise, the V_{OC}^{rad} can be calculated as follows:

$$V_{OC}^{rad} = \frac{kT}{q}\ln\left(\frac{J_{SC}}{J_0^{rad}} + 1\right) = \frac{kT}{q}\ln\left(\frac{q\int_0^\infty EQE_{PV}(E)\emptyset_{AM1.5G}(E)dE}{q\int_0^\infty EQE_{PV}(E)\emptyset_{BB}(E)dE} + 1\right)$$

Where $\emptyset_{BB}(E)$ is the black body spectrum, given by Planck's law:

$$\emptyset_{BB}(E) = \frac{2\pi E^2}{h^3c^2}\frac{1}{\left[exp\left(\frac{E}{kT}\right) - 1\right]} \approx \frac{2\pi E^2}{h^3c^2}exp\left(\frac{-E}{kT}\right)$$

Where *h* is Planck's constant, and *c* is the light speed in the vacuum.

When using the ideal external quantum efficiency $EQE_{PV}^{SQ}(E)$ to replace $EQE_{PV}(E)$, the corresponding result is V_{OC}^{SQ} instead of V_{OC}^{rad}, when using the actual external quantum efficiency $EQE_{PV}(E)$ of the device, the result is V_{OC}^{rad}.

In summary, we can obtain these three terms of energy losses from experiments and calculations:

$\Delta E_1 = E_g - qV_{oc}^{SQ}$

$\Delta E_2 = qV_{OC}^{SQ} - qV_{OC}^{rad}$

And the non-radiative energy loss (ΔE_3) can be calculated by:

$$\Delta E_3 = qV_{OC}^{rad} - qV_{OC}$$

Atomic force microscopy (AFM) measurement**:** AFM measurements were performed with a Nano Wizard 4 atomic force microscopy (JPK Inc. Germany) in Qi mode to observe the film surface morphologies of the Glass/PEDOT:PSS/Active layer.

Transmission electron microscopy (TEM) measurement**:** TEM measurements were carried out using a 200 kV (JEOL ARM-200F). Samples for TEM were prepared on a Cu mesh grid.

Grazing incidence X-ray scattering (GIWAXS) measurement**:** GIWAXS measurement was carried out with a Xeuss 2.0 SAXS/WAXS laboratory beamline using a Cu X-ray source (8.05 keV, 1.54 Å) and a Pilatus3R 300K detector. The incident angle was 0.13°. The samples for GIWAXS measurements were fabricated on silicon substrates.

Photo-stability testing: All the fabrication process is consistent with what is mentioned above. The binary and quaternary devices were illuminated using a white LED array (Cree XLamp-CXA1512, the color temperature is 5000 K) with an output light intensity adjusted to generate a similar photocurrent with the value under the solar simulator. The light-soaking tests were calibrated by the light meter (TES-1332A, TES Electrical Electronic Corp.). We tested the degradation trends of the corresponding devices under continuous solar simulator illumination at maximum power point for 400 hours, the error bars were calculated from eight independent devices.

Outdoor stability testing: The devices were prepared using the same process as above, we used a larger ITO substrate (2.5 × 2.5 cm^2) to allow for encapsulation. The effective area of the active layers is 0.05 cm^2. The devices were encapsulated using UV-curable adhesive and glass slides in a nitrogen atmosphere and cured using UV LED irradiation for one hour. The devices underwent two days of dark state storage in a glove box before outdoor stability testing. Outdoor stability tests were performed on a self-made setup placed in an open and unobstructed field (in Wuhan University campus, Hubei Province, China, the latitude and longitude coordinates are 114°21'20"N, 30°32'20"E). Organic solar cells were placed on the test setup at a fixed angle (30° elevation towards the south) without a sun tracker. The devices and test circuits were exposed to the ambient air and the cells were scanned for voltage-current at 6-min intervals. Current-voltage curves were measured and recorded by a Keithley 2400 source meter. The devices were kept at an open circuit state when not scanning. The whole test followed the existing ISOS-O-2 protocol.

Light spectrum measuring: Relative spectral power distribution curves of the LED light and the sunlight for the aging tests are measured with a fiber optic spectrometer (Ocean Optics QE65 Pro Spectrometer). The raw data is collected in the form of photon numbers and wavelengths, and are converted into energy distributions. The solar spectrum is obtained by sampling using an optical fiber facing the sun at noon in Wuhan, China. The spectral distribution of the actual irradiation to the device surface will be different depending on factors such as atmospheric absorption, and the ratio of direct radiation to scattered radiation.

Weather information collection: The temperatures in the vicinity of the device are recorded by a DS18B20-type digital thermometer, and measurements are triggered synchronously during each current-voltage scan of the device. Air temperatures were obtained from local weather stations at one-hour sampling intervals. Solar radiation density was recorded by a calibrated monocrystalline silicon solar cell, which was held in an orientation parallel to the organic solar cells.

Pseudo-free-standing tensile measurement**:** For the tensile testing specimen, the active layers were blade-coated onto the PEDOT:PSS/glass substrate. The active layer specimen with a size of 1.2×0.5 cm^2 was prepared by using a cutting plotter. To float the specimen on the water surface, water was allowed to penetrate the PEDOT: PSS layer. Subsequently, PEDOT: PSS was dissolved, and the active layer was delaminated from the glass substrate. By performing this process at the water surface, the floating active layer specimen could be obtained. Specimen gripping was achieved by attaching PDMS-coated Al grips on the specimen gripping areas using van der Waals adhesion. The tensile test was performed by a linear stage with a strain rate of 0.1 mm/s. During the tensile test, stress and strain data were obtained through a load cell (KYOWA) and a digital image correlation (DIC) device, respectively. All tensile tests were carried out under ambient conditions (Temperature ~ 25 ℃, relative humidity (RH) ~ 30 %).

2. Figures and Tables

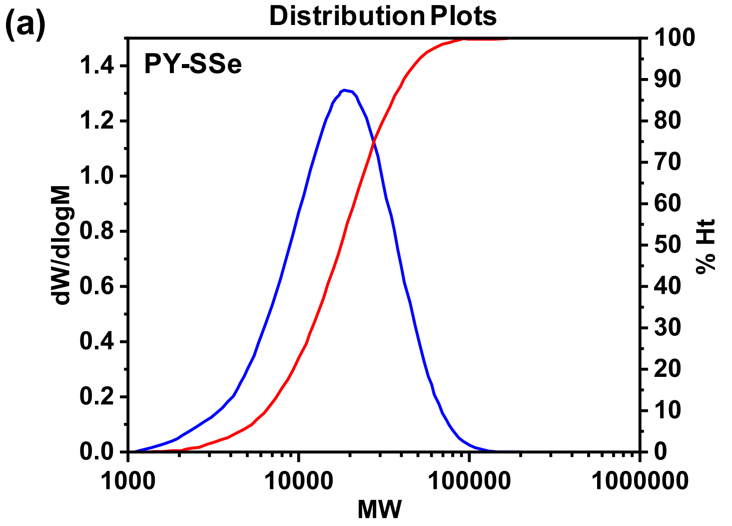

MW Averages
Mp: 18938 Mn: 12082 Mv: 19271 Mw: 20624
Mz: 30965 Mz+1: 42668 PD: 1.7070

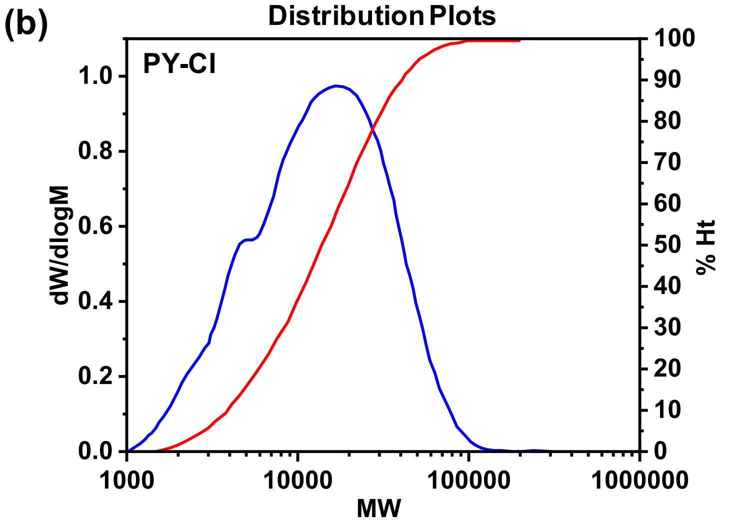

MW Averages
Mp: 16959 Mn: 8528 Mv: 16473 Mw: 18174
Mz: 31612 Mz+1: 45541 PD: 2.1311

Figure S1. Molecular weight values of PY-SSe and PY-Cl polymer acceptors obtained by GPC with 1,2,4-trichlorobenzeneas the eluent at 150 °C.

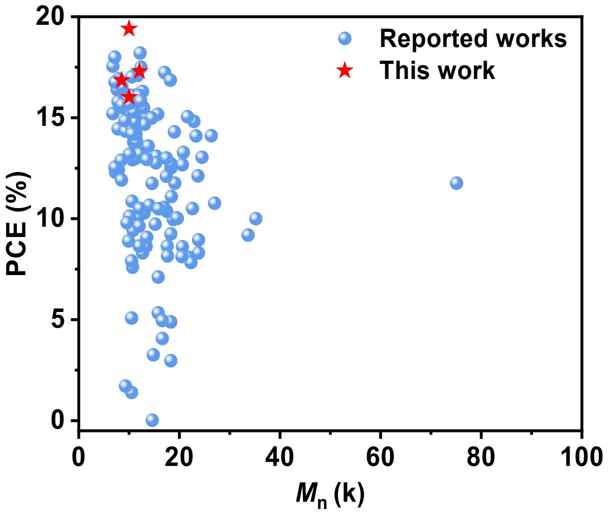

Figure S2. Summary of the PCE as a function of the P_A's number-average molecular weight extracted from the reported all-PSCs and this work.

Table S1. Optimized PCE and number-average molecular weights (M_n) of polymer acceptors for some of the all-polymer systems reported in the literature.

Acceptor M_n (k)	Optimal PCE (%)	Materials (Donor:Acceptor)	Reference
33.65	9.19	PBDB-T:PZ1	[4]
35.2	10	PM6:PFBDT-IDTIC	[5]
22.6	10.5	PM6:PN1	[6]
23.8	8.31	PM6:PF2-DTC	[7]
27	10.77	PM6:PF2-DTSi	[7]
21.8	8.09	PM6:PF2-DTGe	[7]
7.3	12.3	PBDB-T:PJ1-L	[8]
11	13.2	PBDB-T:PJ1-M	[8]
23.3	14.1	PBDB-T:PJ1-H	[8]
7.9	12.41	PBDB-T:PF5-Y5-low	[9]
13	10.28	PBDB-T:PF5-Y5-mid	[9]
7.8	14.45	PBDB-T:PF5-Y5-high	[9]
7.2	12.55	PM6:PYT-L	[10]
12.3	13.44	PM6:PYT-M	[10]
20.6	8.61	PM6:PYT-H	[10]
23.8	8.95	PM6:PF2-DTC	[11]
22.3	7.83	PM6:PF3-DTC	[11]
11.9	10.13	PM6:PF3-DTCO	[11]
18.8	9.96	PBDB-T:PTPBT	[12]
17.5	10.37	PBDB-T:PTPBT-ET-0.1	[12]
19.1	11.76	PBDB-T:PTPBT-ET-0.2	[12]
18.33	12.52	PBDB-T:PTPBT-ET-0.3	[12]
16.9	10.56	PBDB-T:PTPBT-ET-0.4	[12]
15.2	9.73	PBDB-T:PTPBT-ET-0.5	[12]
10.5	5.08	PBDB-T:PTPBT-ET-0.75	[12]

75.1	11.76	PTzBI-Si:N2200	[13]
18.3	2.97	PBDB-T:PIDIC2T	[14]
16.6	4.07	PBDB-T:PIDIC2T2F	[14]
15.8	5.34	PBDB-T:PIDIC2T2Cl	[14]
18.3	4.89	PM6:PIDIC2T	[14]
16.6	4.96	PM6:PIDIC2T2F	[14]
15.8	7.11	PM6:PIDIC2T2Cl	[14]
10.7	7.6	PBDB-T:Y5-Se-Out	[15]
17.6	8.65	PBDB-T:Y5-Se-Mix	[15]
10.7	12.92	PBDB-T:Y5-Se-In	[15]
10.1	10.13	PBDB-T:Y5-BiSe-Out	[15]
10.8	9.42	PBDB-T:Y5-BiSe-Mix	[15]
12.7	8.31	PBDB-T:Y5-BiSe-In	[15]
13.4	8.63	PM6:PF1-TS4	[16]
18.4	11.1	PM6:L11	[17]
19	14.3	PM6:L14	[17]
20.6	12.67	PBDB-T:PYE0	[18]
15.4	13.09	PBDB-T:PYE10	[18]
13.8	13.6	PBDB-T:PYE20	[18]
20.8	13.28	PBDB-T:PYE30	[18]
24.5	13.04	PBDB-T:PYE40	[18]
13.35	15.11	PTzBI-oF:PFA1	[19]
10.9	13.8	PTzBI-oF:PS1	[20]
12	8.65	PBDB-T:P(BDT2BOY5-H)	[21]
12	9.64	PBDB-T:P(BDT2BOY5-F)	[18]
14	10.67	PBDB-T:P(BDT2BOY5-Cl)	[18]
11.4	14.6	PBDB-T-LW:PJ1	[22]
11.4	15.4	PBDB-T-MW:PJ1	[22]

11.4	13	PBDB-T-HW:PJ1	[22]
12.1	13.22	PBDB-T:PYN-BDTF	[23]
13.5	9.08	PM6:PYN-BDTF	[23]
15.7	15.17	PBDB-T:PYT	[24]
19.6	10.02	PM6:PCl	[25]
18.3	9.25	PM6:PCl-Si	[25]
11	14	PM6:PYF-T	[26]
11.1	15.2	PM6:PYF-T-o	[26]
10.5	1.4	PM6:PYF-T-m	[26]
8.5	11.92	PM6:PBTIC-γ-2F2T	[27]
9.3	14.34	PM6:PBTIC-m-2F2T	[27]
14.6	0.02	PM6:PBTIC-δ-2F2T	[27]
14.8	3.26	PM6:PBTIC-γ-2T	[27]
14.566	11.75	PBDB-T:PYT	[28]
15.326	12.77	PBDB-T:PYT-TOE(10)	[28]
15.85	10.49	PBDB-T:PYT-TOE(20)	[28]
17.643	8.16	PBDB-T:PYT-TOE(30)	[28]
8.4	12.9	PBDB-T:PYT	[28]
10.6	14.5	PBDB-T:PZT	[28]
7.8	15.8	PBDB-T:PZT-γ	[28]
14.5	14.98	PM6:PY2F-T	[29]
13.5	12.94	PM6:PY-T	[29]
9.6	9.8	PBDB-T:PY-O	[30]
10.89	14.16	PBDB-T:PY-S	[30]
8.96	15.48	PBDB-T:PY-Se	[30]
11.5	13.83	PBDB-T:PS-Se	[31]
11.7	16.16	PBDB-T:PN-Se	[31]
22.9	14.82	PBDB-T:PY5-BTZ	[32]

18.3	12.73	PBDB-T:PY5-2TZ	[32]
17.4	12.1	PBDB-T:PY5-PZ	[32]
20.5	8.12	PBDB-T:PY5-BT	[32]
11.1	14.8	PM6:PY2S-H	[33]
10.4	15.1	PM6:PY2S-F	[33]
12.5	15.6	PM6:PY2Se-F	[33]
10.5	16.1	PM6:PY2Se-Cl	[33]
17.4	13.01	PBDB-T:PYTS-0.0	[34]
11.4	14.19	PBDB-T:PYTS-0.1	[34]
13.1	14.68	PBDB-T:PYTS-0.3	[34]
10.5	7.91	PBDB-T:PYTS-0.5	[34]
9.3	1.71	PBDB-T:PYTS-1.0	[34]
11.1	14.8	PM6:PYT-2S	[35]
12.7	16.3	PM6:PYT-1S1Se	[35]
12.9	15.5	PM6:PYT-2Se	[35]
10.6	10.86	PBQx-Me-TF:PBTIC-γ-TT	[36]
10.6	14.21	PBQx-H-TF:PBTIC-γ-TT	[36]
11.7	17.1	PM6:PY-V-γ	[37]
12.1	16.1	PM6:PY-T-γ	[37]
10.9	15.3	PM6:PY-2T-γ	[37]
11.61	15.77	PBQx-H-TF:PBTIC-γ-TSe	[38]
26.336	14.11	PM6:PY-IT2F	[39]
11.941	16.09	PM6:PG-IT	[39]
17.073	17.24	PM6:PG-IT2F	[39]
12.1	10.51	PBQx-TCl:PBTPICm-BDD	[40]
12.38	17.5	PBQx-TCl:PBTPICγ-BDD	[40]
11.6	17.17	PBQx-TCl:PBTPICF-BDD	[40]
7.9	16.92	PM6:PYDT	[41]

6.8	17.55	PM6:PYDT-CzP-9	[41]
6.8	15.21	PM6:PYDT-CzP-15	[41]
23.7	12.12	PM6:PY-IT	[42]
21.6	15.05	PM6:PY-OT	[42]
19.5	10.04	PM6:PY-IOT	[42]
8.56	15.65	PM6:PW-Se	[43]
9.9	8.9	PM6:PS-Se	[43]
10.1	13.2	PM6:PYT	[44]
10	15.7	PM6:PY-DF	[44]
10.53	17.03	PM6:PY-SSe-V	[45]
8.53	16.37	PM6:PY-Cl	[45]
7.16	18	PQM-Cl:PY-IT	[46]
18.2	16.86	PM6:PYT-1S1Se	[47]
12.3	15.83	PM6:PYT-1S1Se-4Cl	[47]
7.6	16.41	PM6:PY-HD	[48]
8.6	16.53	PM6:PY-OD	[48]
7.2	16.76	PM6:PY-DT	[48]
9.2	14.86	PM6:PY-DH	[48]

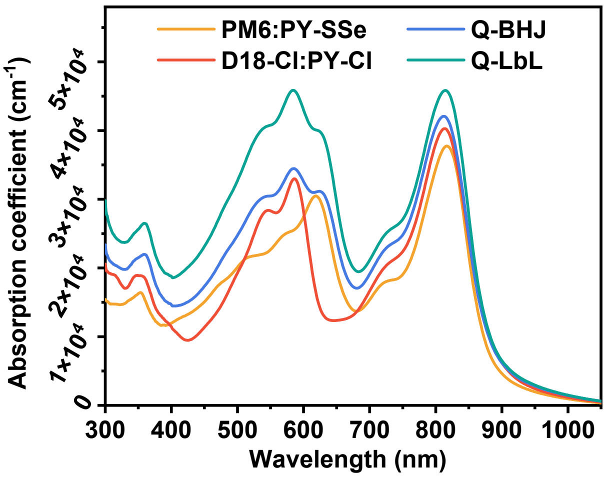

Figure S3. Absorption coefficients of the PM6:PY-SSe, D18-Cl:PY-Cl, Q-BHJ and Q-LbL blend films.

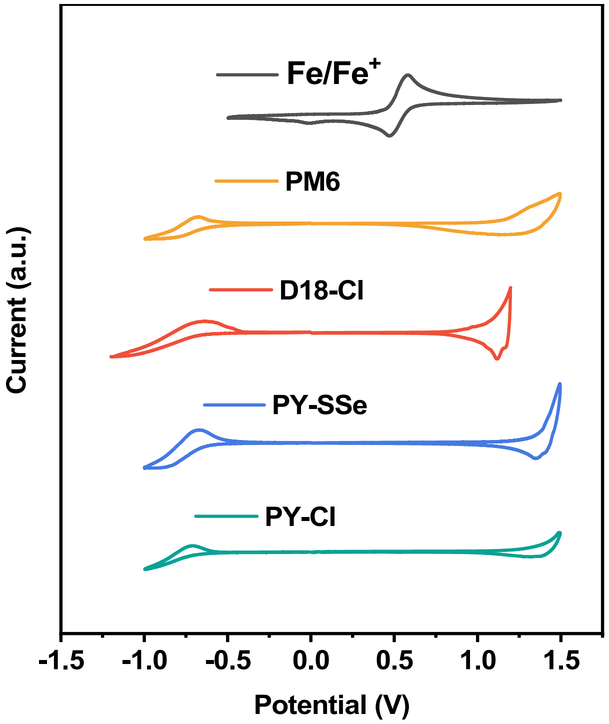

Figure S4. Cyclic voltammetry curves of Fc/Fc+, PM6, D18-Cl, PY-SSe, and PY-Cl in acetonitrile solution with 0.1 Mn-Bu$_4$PF$_6$ as the supporting electrolyte, with a scanning rate of 100 mV s^{-1}.

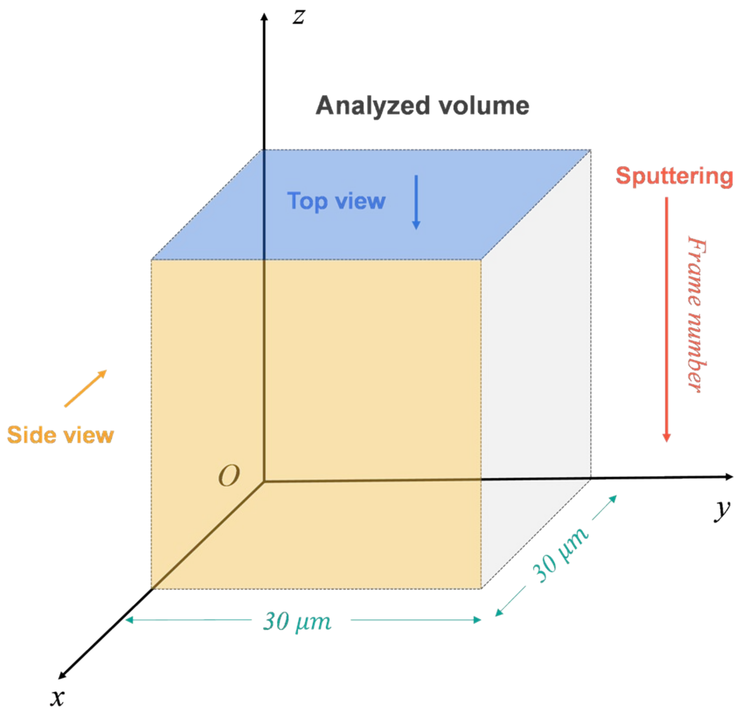

Figure S5. Schematic diagram of the top view map and side view map of the analyzed volume in the TOF-SIMS test. The top view plane (blue) is parallel to the substrate, while the side view plane (yellow) is perpendicular to the substrate. The red arrow represents the sputtering direction, along this direction, the tested films were etched frame by frame by the ion beam and were used for secondary ion mass spectrometry analysis.

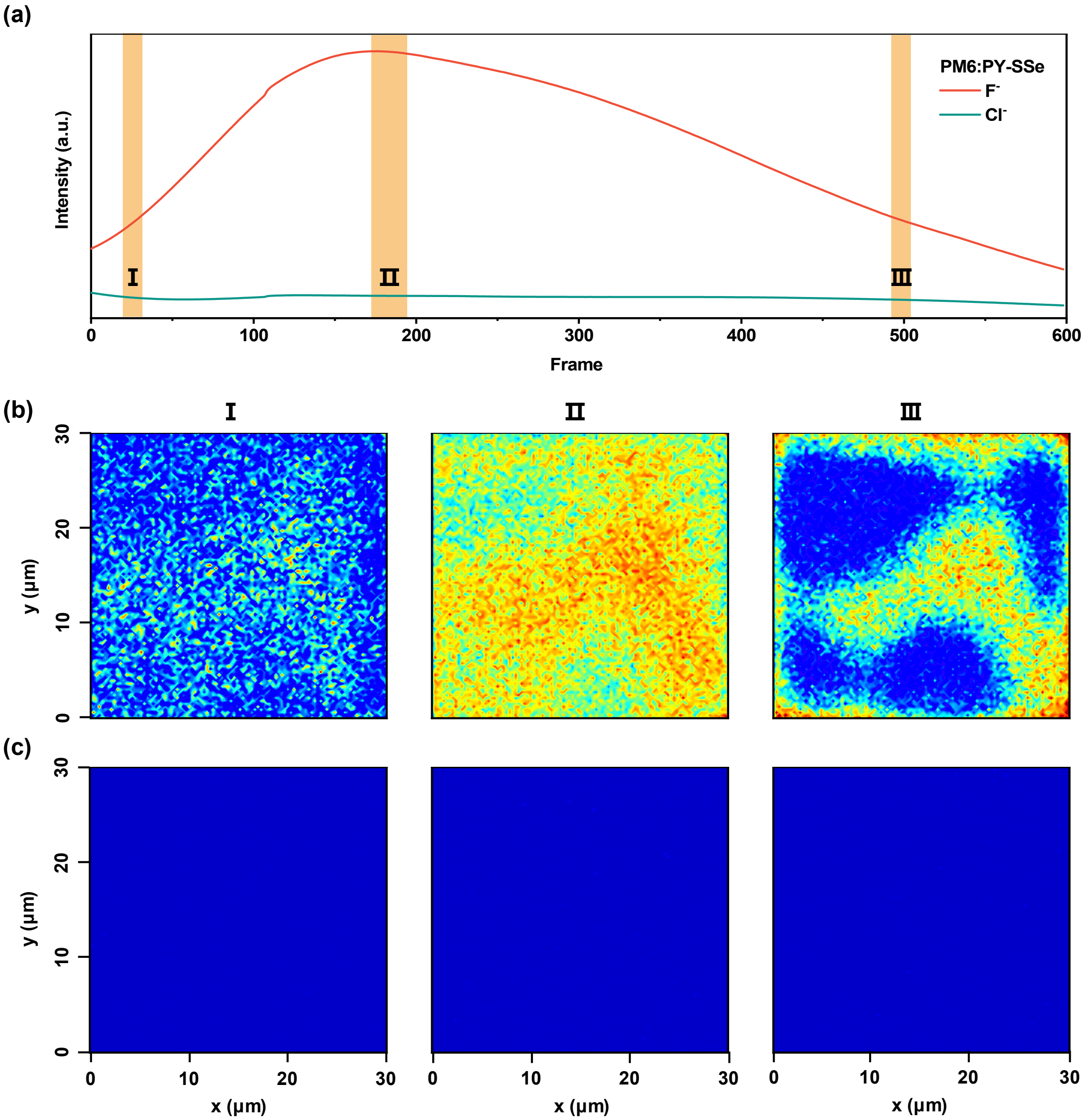

Figure S6. (a) TOF-SIMS ion yield as a function of sputtering time for PM6:PY-SSe samples. The depth profile of F^- and Cl^- ions is shown here. Top view of (b) F^- signals and (c) Cl^- signals at the top (region I), middle (region II) and bottom (region III) part of the whole active layer.

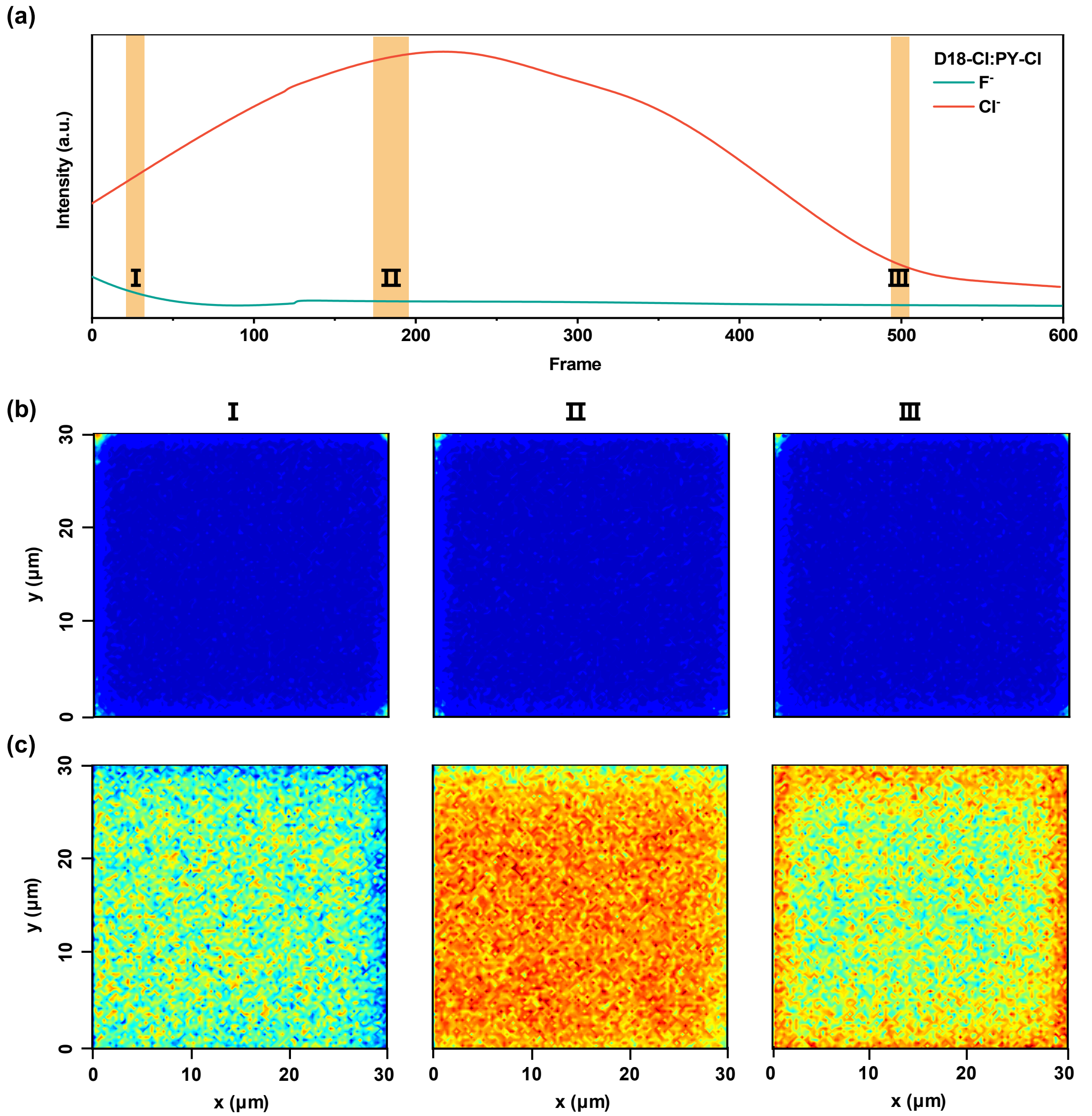

Figure S7. (a) TOF-SIMS ion yield as a function of sputtering time for D18-Cl:PY-Cl samples. The depth profile of F^- and Cl^- ions is shown here. Top view of (b) F^- signals and (c) Cl^- signals at the top (region I), middle (region II) and bottom (region III) part of the whole active layer.

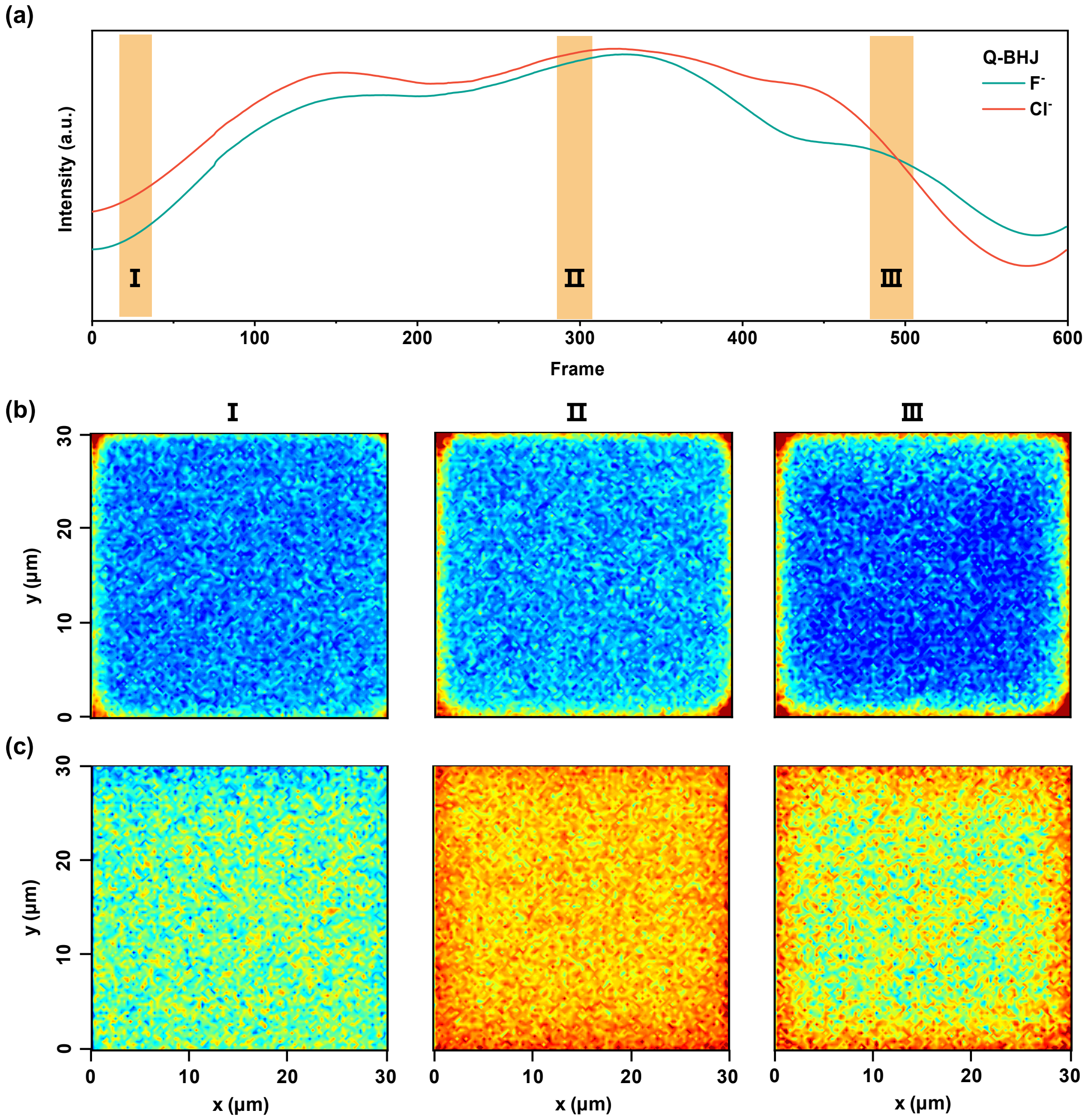

Figure S8. (a) TOF-SIMS ion yield as a function of sputtering time for Q-BHJ samples. The depth profile of F^- and Cl^- ions is shown here. Top view of (b) F^- signals and (c) Cl^- signals at the top (region I), middle (region II) and bottom (region III) part of the whole active layer.

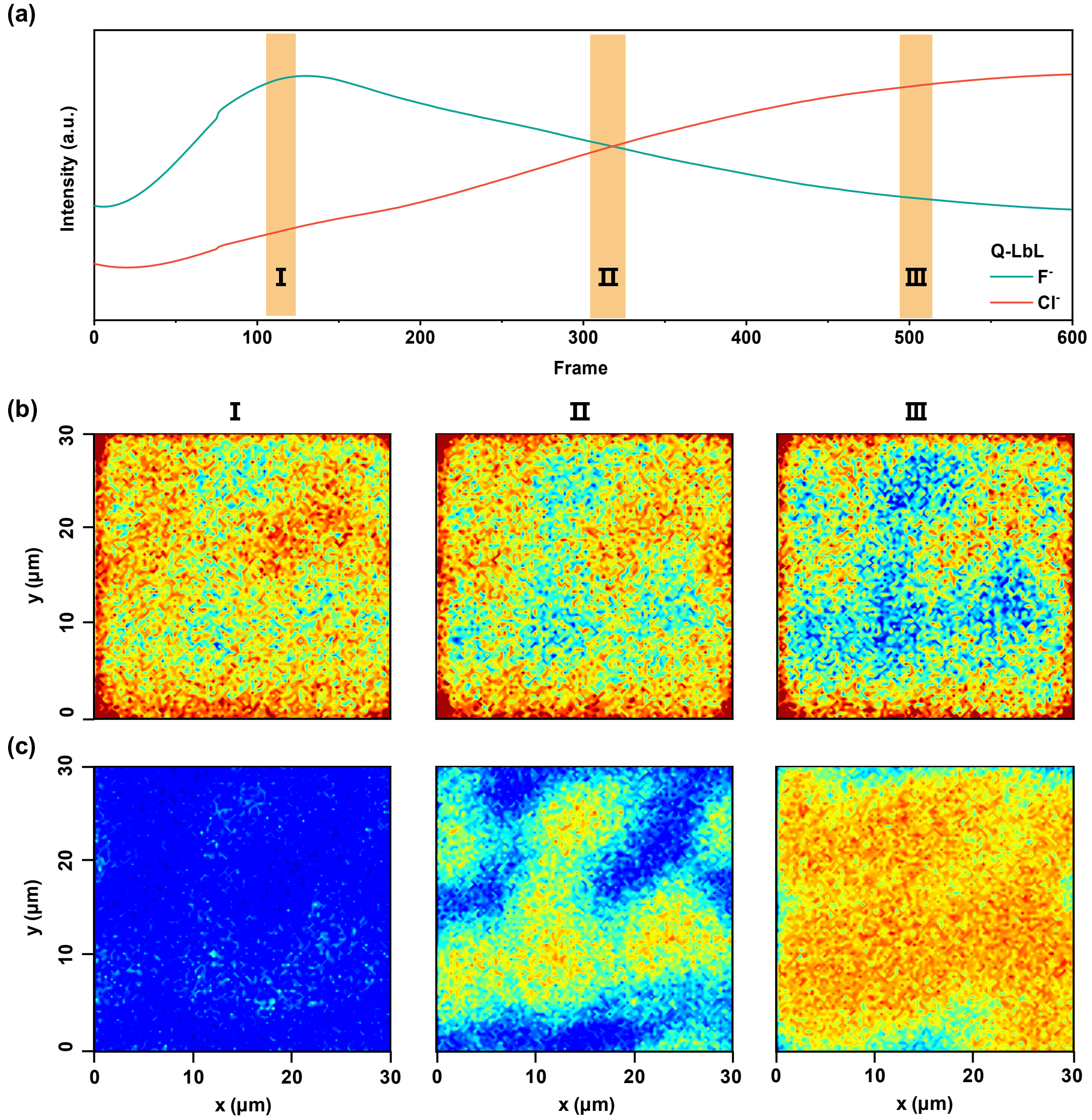

Figure S9. (a) TOF-SIMS ion yield as a function of sputtering time for Q-LbL samples. The depth profile of F^- and Cl^- ions is shown here. Top view of (b) F^- signals and (c) Cl^- signals at the top (region I), middle (region II) and bottom (region III) part of the whole active layer.

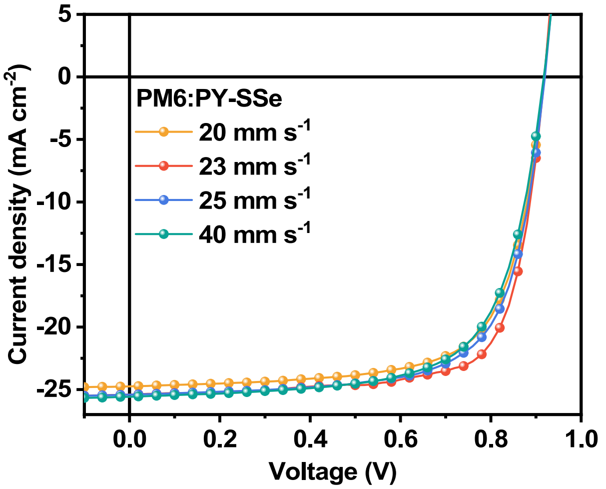

Figure S10. *J*-*V* curves of the devices based on PM6:PY-SSe with varying coating speed, measured under the illumination of AM 1.5 G at 100 mW cm^{-2}.

Table S2. Photovoltaic parameters of devices based on PM6:PY-SSe with varying coating speed, measured under the illumination of AM 1.5G at 100 mW cm^{-2}.

Speed [mm s^{-1}]	Thickness [nm]	V_{OC} [V]	J_{SC} [mA cm^{-2}]	FF [%]	PCE$^{a)}$ [%]
20	85	0.918	24.75	70.25	15.96 (15.62±0.14)
23	101	0.919	25.39	74.17	17.31 (17.12±0.12)
25	127	0.919	25.40	70.03	16.35 (16.05±0.08)
28	140	0.917	25.58	68.09	15.97 (15.64±0.10)

[a]The values in the square bracket are the average PCE obtained from eight devices.

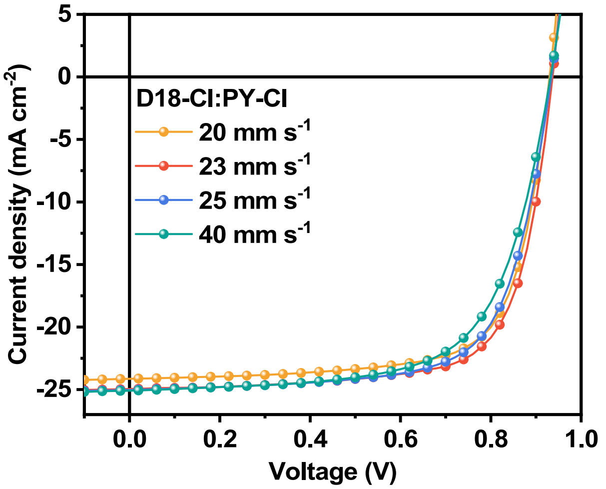

Figure S11. *J-V* curves of the devices based on D18-Cl:PY-Cl with varying coating speed, measured under the illumination of AM 1.5G at 100 mW cm^{-2}.

Table S3. Photovoltaic parameters of devices based on D18-Cl:PY-Cl with varying coating speed, measured under the illumination of AM 1.5G at 100 mW cm^{-2}.

Speed [mm s^{-1}]	Thickness [nm]	V_{OC} [V]	J_{SC} [mA cm^{-2}]	FF [%]	PCE$^{a)}$ [%]
20	78	0.934	24.14	71.77	16.18 (15.89±0.13)
23	105	0.937	24.95	72.10	16.85 (16.62±0.08)
25	129	0.934	25.02	69.77	16.30 (16.03±0.12)
28	142	0.932	25.09	66.13	15.20 (14.95±0.10)

[a]The values in the square bracket are the average PCE obtained from eight devices.

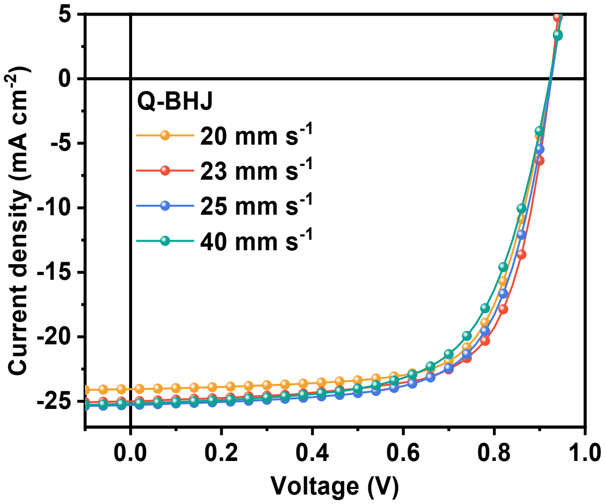

Figure S12. *J-V* curves of the devices based on Q-BHJ with varying coating speed, measured under the illumination of AM 1.5G at 100 mW cm^{-2}.

Table S4. Photovoltaic parameters of devices based on Q-BHJ with varying coating speed, measured under the illumination of AM 1.5G at 100 mW cm^{-2}.

Speed [mm s^{-1}]	Thickness [nm]	V_{OC} [V]	J_{SC} [mA cm^{-2}]	FF [%]	PCE$^{a)}$ [%]
20	84	0.923	24.06	69.50	15.43 (15.13±0.15)
23	110	0.924	25.00	69.33	16.02 (15.75±0.17)
25	132	0.926	25.29	67.52	15.81 (15.56±0.07)
28	146	0.922	25.18	64.35	14.94 (14.65±0.11)

[a] The values in the square bracket are the average PCE obtained from eight devices.

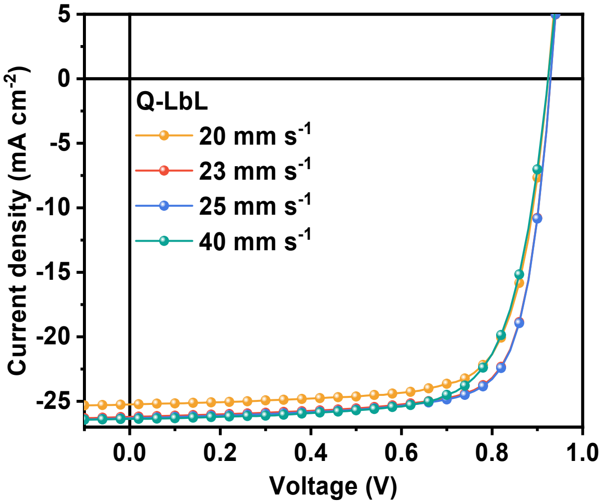

Figure S13. *J-V* curves of the devices based on Q-LbL with varying coating speed, measured under the illumination of AM 1.5G at 100 mW cm^{-2}.

Table S5. Photovoltaic parameters of devices based on Q-LbL with varying coating speed, measured under the illumination of AM 1.5G at 100 mW cm^{-2}.

Speed [mm s^{-1}]	Thickness [nm]	V_{OC} [V]	J_{SC} [mA cm^{-2}]	FF [%]	PCE$^{a)}$ [%]
20	82	0.924	25.25	74.31	17.32 (17.06±0.09)
23	102	0.930	26.60	78.65	19.46 (19.18±0.10)
25	127	0.924	26.31	74.13	18.02 (17.70±0.15)
28	145	0.924	26.36	72.36	17.62 (17.44±0.10)

[a]The values in the square bracket are the average PCE obtained from eight devices.

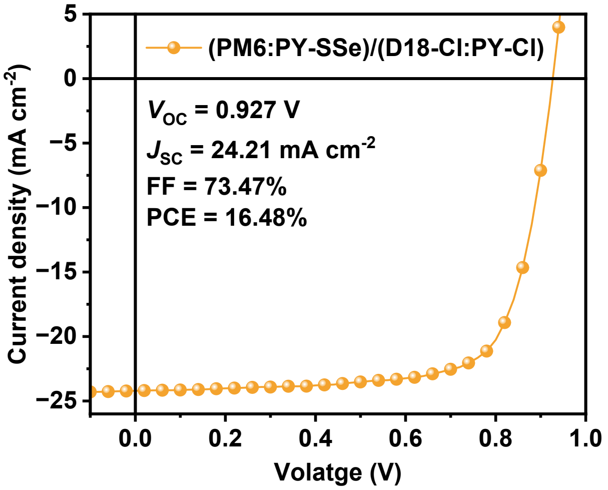

Figure S14. *J*-*V* curves of the devices based on Q-LbL with (PM6:PY-SSe)/(D18-Cl:PY-Cl) structure, measured under simulated illumination of AM 1.5 G at 100 mW cm^{-2}.

Table S6. Data points gathered from published studies on all-polymer solar cells processed by printing technology. The publication years, photovoltaic parameters, champion PCEs and materials used are summarized below. The corresponding references can be found at the end of the supporting information.

Year	V_{OC} (V)	J_{SC} (mA cm^{-2})	FF (%)	PCE (%)	Systems	Reference
2015	1.01	7.04	46	3.27	PII-tT-PS5:P(TP)	[49]
2015	0.98	8.14	43	3.42	PII-tT:P(TP)	[49]
2017	0.64	15.5	50	5.10	PTB7-Th:PPDIE	[50]
2018	0.95	18.14	66	11.70	PBTA-TF:IT-M	[51]
2019	0.95	18.1	73.6	12.70	FTAZ:PBDB-T:IT-M	[52]
2019	0.88	17.62	75.58	11.76	PTzBI-Si:N2200	[53]
2019	0.94	17.05	69	11.14	PBDB-T:IT-M	[54]
2020	0.92	16.5	67.2	10.15	PBDB-T:IT-M	[55]
2021	0.787	11.2	51	4.50	PTB7-Th:P(NDI2OD-2T)	[56]
2021	0.891	23.03	73.98	15.17	PBDB-T:PYT	[57]
2021	1.25	8.31	53.8	5.59	CD1:PBN-21	[58]
2021	0.901	22.6	63.4	13.0	PM6:PYF-T-o	[59]
2022	0.874	19.4	53.9	9.14	PBDB-T:PYSe	[60]
2022	0.894	21.3	62.2	11.84	PBDB-T:PYSe-TCl20	[60]
2022	0.908	22.3	68.1	12.83	PBDB-T:PYSe-TCl20:PTClo-Y	[60]
2022	0.948	19.99	65.7	12.42	Y5-Br:PTClo-Y	[61]
2022	0.89	23.05	65.52	13.44	PM6:PBN26	[62]
2022	0.891	22.94	66.26	13.54	PBDB-T:PYSe-TC6T (10)	[63]
2022	0.945	23.27	70.77	15.53	PM6:PY-IT	[64]
2022	0.94	13.09	52.1	6.43	PBDBT:PF5-Y5	[65]
2023	0.92	15.7	60	8.66	PBDBT:PF5-Y5	[66]

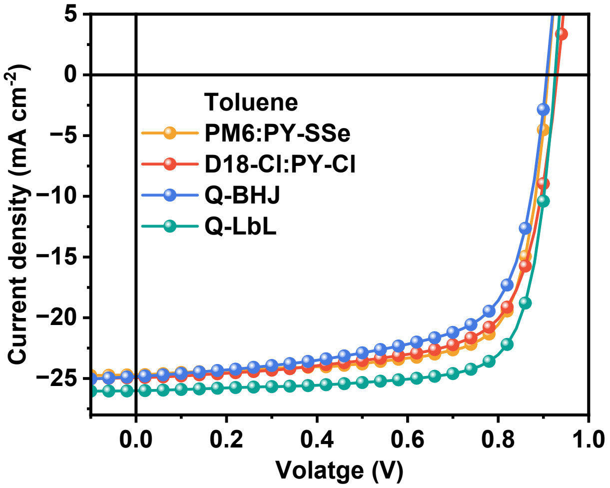

Figure S15. *J-V* curve statistics of relevant devices fabricated with toluene solvent under the illumination of AM 1.5G at 100 mW cm^{-2}.

Table S7. Photovoltaic parameters of relevant devices fabricated with toluene solvent under the illumination of AM 1.5G at 100 mW cm^{-2}.

Active layer	Thickness [nm]	V_{OC} [V]	J_{SC} [mA cm^{-2}]	FF [%]	PCE$^{a)}$ [%]
PM6:PY-SSe	108	0.911	24.70	74.04	16.64 (16.36±0.14)
D18-Cl:PY-Cl	112	0.930	24.94	69.87	16.21 (15.98±0.10)
Q-BHJ	105	0.907	24.84	67.75	15.27 (15.04±0.15)
Q-LbL	110	0.926	26.02	76.53	18.43 (18.16±0.09)

[a] The values in square bracket are the average PCE obtained from eight devices.

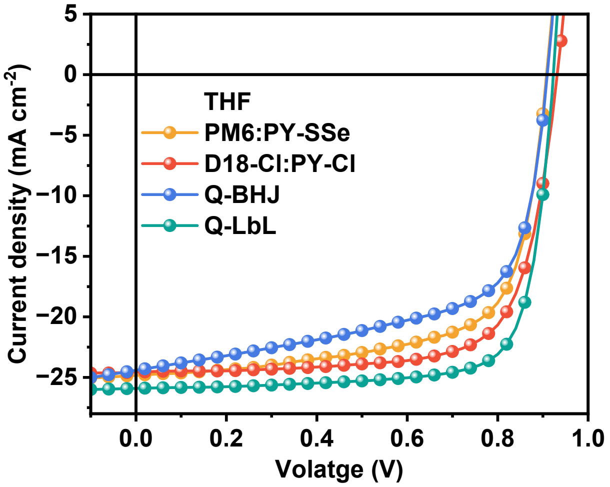

Figure S16. *J-V* curve statistics of relevant devices fabricated with THF solvent under the illumination of AM 1.5G at 100 mW cm^{-2}.

Table S8. Photovoltaic parameters of relevant devices fabricated with THF solvent under the illumination of AM 1.5G at 100 mW cm^{-2}.

Active layer	Thickness [nm]	V_{OC} [V]	J_{SC} [mA cm^{-2}]	FF [%]	PCE$^{a)}$ [%]
PM6:PY-SSe	104	0.908	24.83	68.13	15.36 (15.20±0.08)
D18-Cl:PY-Cl	106	0.932	24.57	72.87	16.69 (16.40±0.12)
Q-BHJ	105	0.910	24.41	62.74	13.93 (13.75±0.08)
Q-LbL	101	0.923	25.91	77.23	18.47 (18.14±0.15)

^{a}The values in square bracket are the average PCE obtained from eight devices.

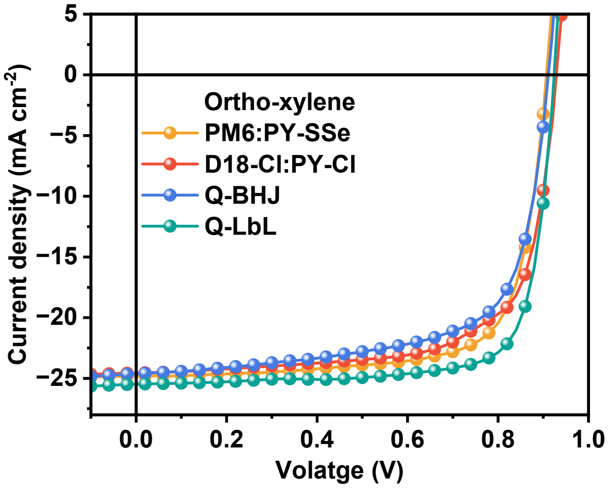

Figure S17. *J-V* curve statistics of relevant devices fabricated with ortho-xylene solvent under the illumination of AM 1.5G at 100 mW cm^{-2}.

Table S9. Photovoltaic parameters of relevant devices fabricated with ortho-xylene solvent under the illumination of AM 1.5G at 100 mW cm^{-2}.

Active layer	Thickness [nm]	V_{OC} [V]	J_{SC} [mA cm^{-2}]	FF [%]	PCE[a)] [%]
PM6:PY-SSe	104	0.907	24.83	73.73	16.60 (16.22±0.20)
D18-Cl:PY-Cl	105	0.929	24.45	69.11	15.70 (15.50±0.12)
Q-BHJ	108	0.911	24.62	68.00	15.25 (15.06±0.09)
Q-LbL	106	0.924	25.48	77.70	18.29 (18.02±0.08)

[a]The values in square bracket are the average PCE obtained from eight devices.

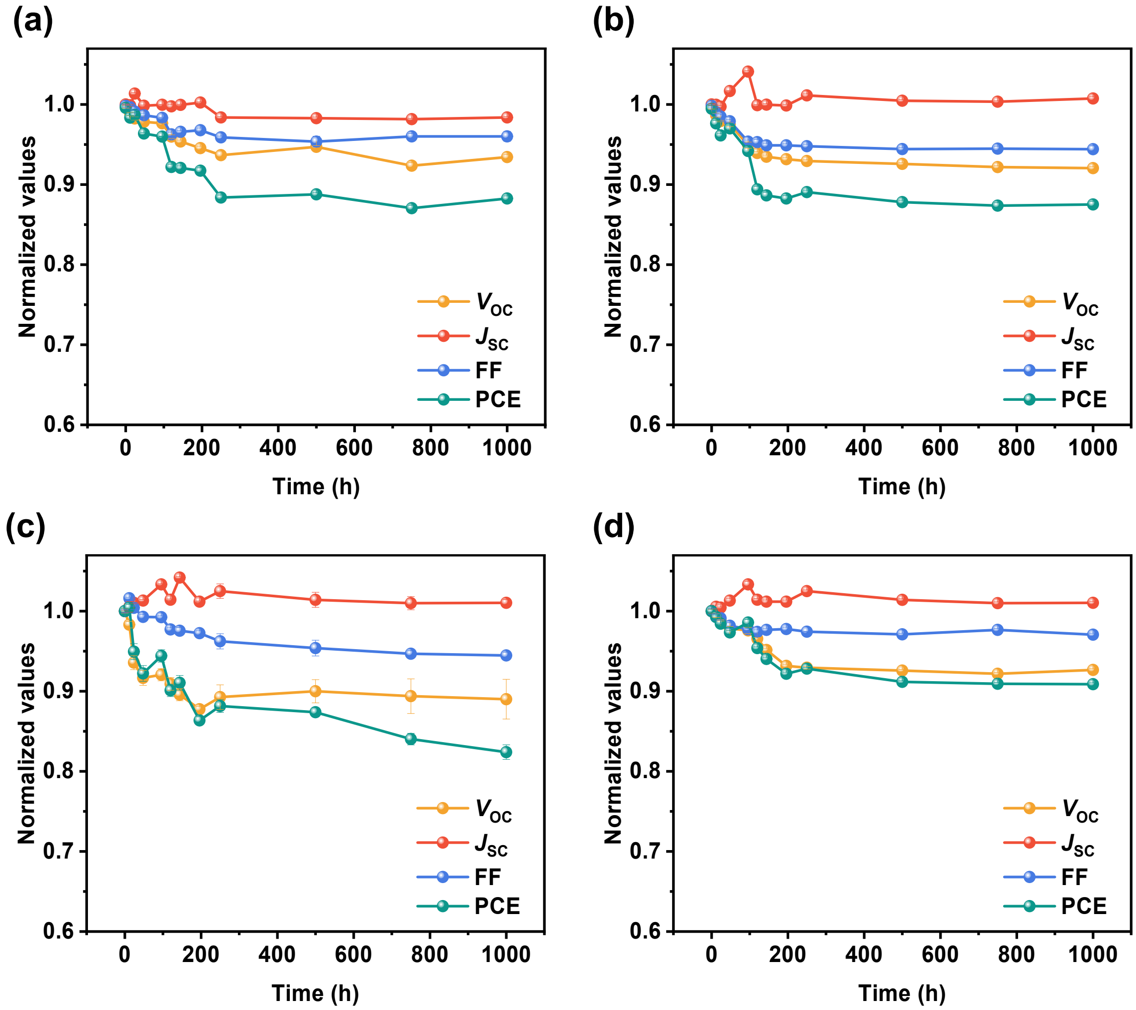

Figure S18. Normalized photovoltaic parameters, including V_{OC}, J_{SC}, FF and PCE of relevant all-polymer blend films ((a) PM6:PY-SSe, (b) D18-Cl:PY-Cl, (c) Q-BHJ and (d) Q-LbL) as a function of time under continues heating at 120 °C.

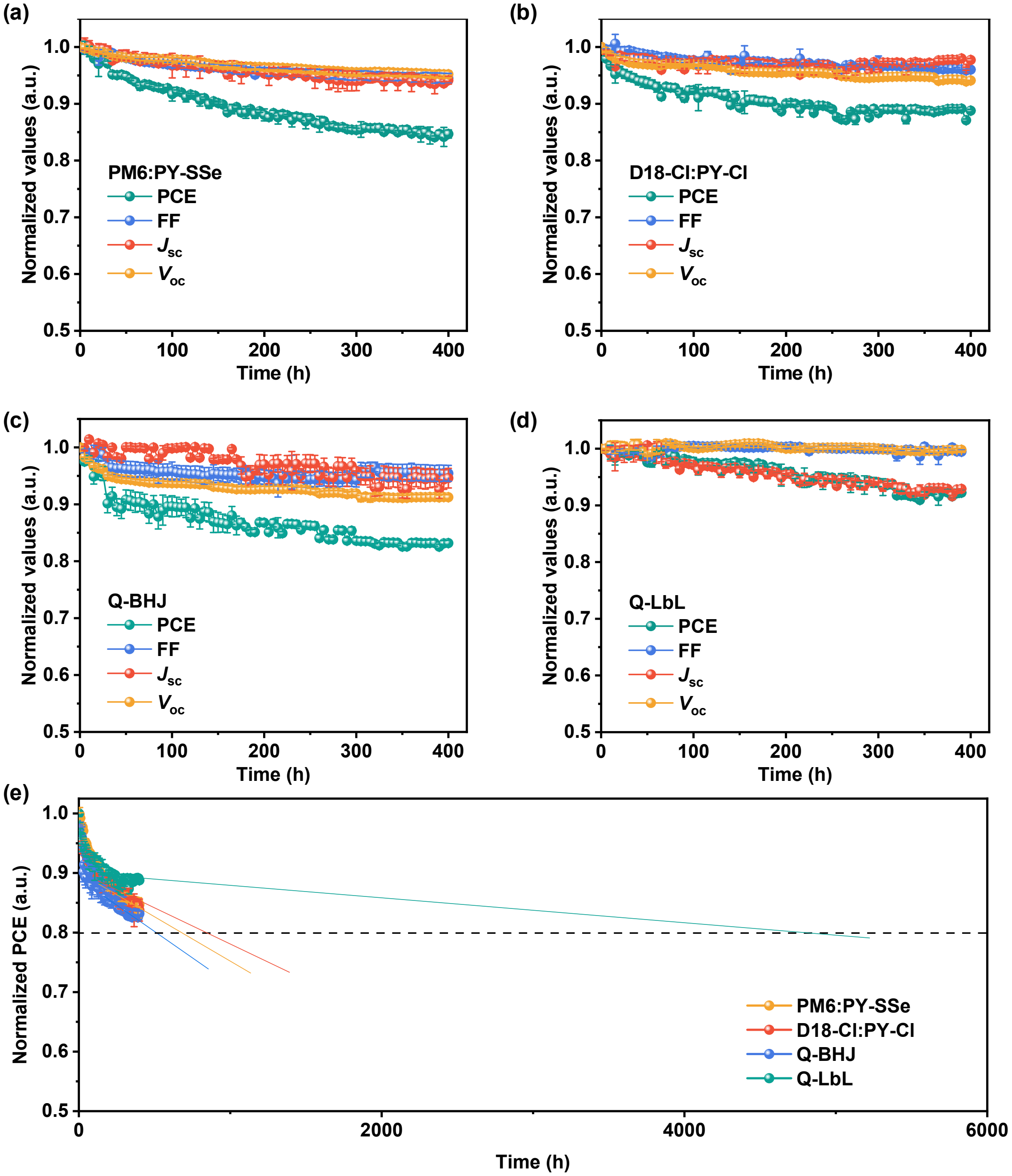

Figure S19. Normalized photovoltaic parameters, including V_{OC}, J_{SC}, FF and PCE of relevant all-PSCs ((a) PM6:PY-SSe, (b) D18-Cl:PY-Cl, (c) Q-BHJ and (d) Q-LbL) as a function of time, measured under continuous LED illumination with intensity equivalent to 1 sun. The all-PSC devices are maintained at maximum power output point during the test. (e) T_{80} lifetime analysis of relevant all-PSCs, obtained by extrapolation method.

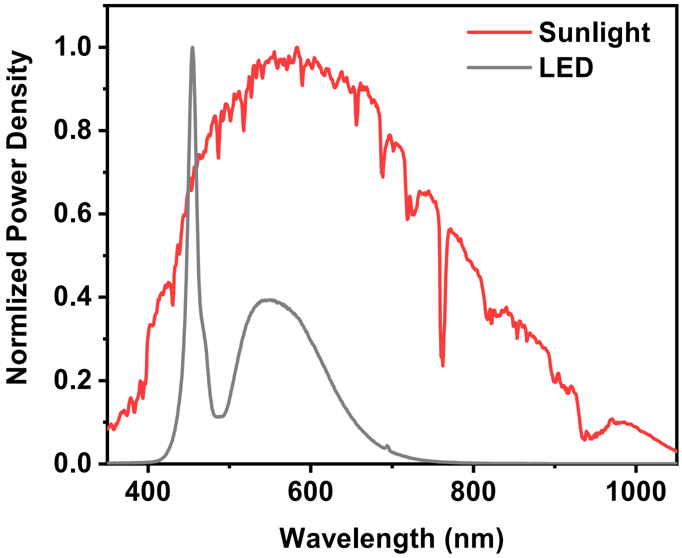

Figure S20. Relative spectral power distribution of the LED light and the sunlight for the aging tests.

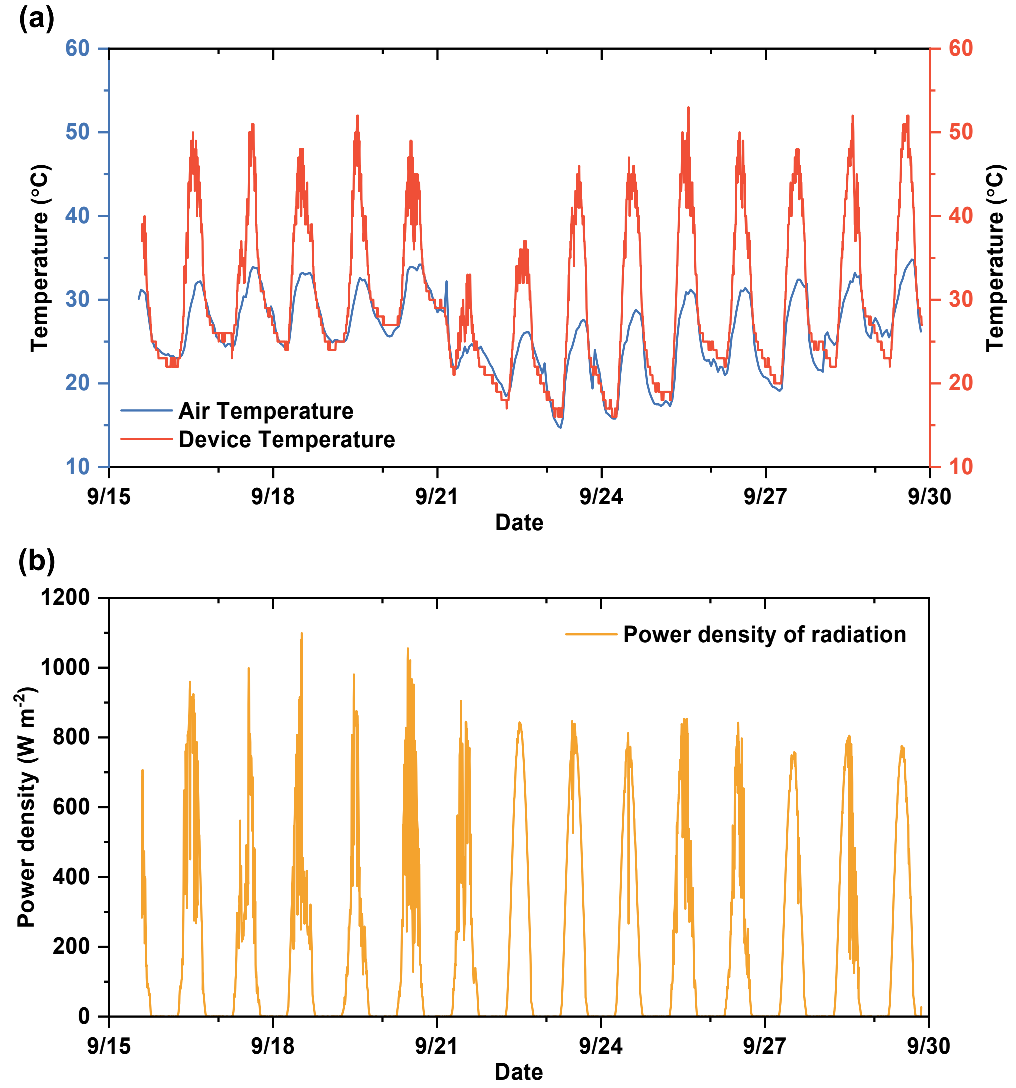

Figure S21. (a) Air temperature (blue line) and temperature in the vicinity of the device (red line) during the outdoor testing. (b) Solar power density as a function of time during the outdoor testing. The noise exhibited in the data during the daytime hours comes mainly from the effect of localized radiated power variations in cloudy conditions.

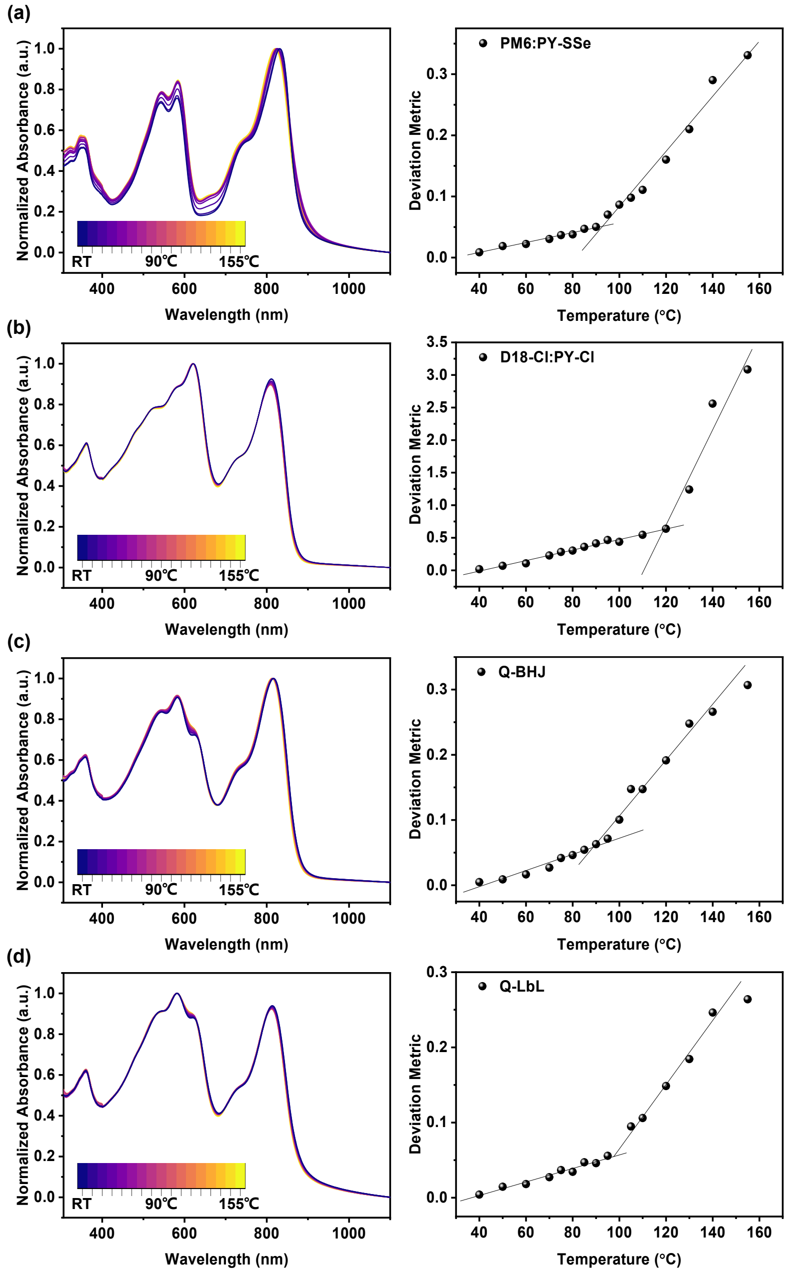

Figure S22. *UV–vis-NIR* absorption spectra of (a) PM6:PY-SSe (b) D18-Cl:PY-Cl, (c) Q-BHJ and (d) Q-LbL. Evolution of the deviation metric (DM_T) as a function of annealing temperature, illustrating a glass transition of PM6:PY-SSe (88.5 ± 1 °C), D18-Cl:PY-Cl (104.8 ± 1 °C), Q-BHJ (90.2 ± 1 °C) and Q-LbL (105.3 ± 1 °C). Notably, the DM_T factor represents the sum of squared deviations in absorbance between un-annealed and annealed films:[67,68]

$$DM_T = \sum_{\lambda_{min}}^{\lambda_{max}} [(I_{RT}(\lambda) - I_T(\lambda)]^2$$

, where λ, $\lambda_{\min}$ and $\lambda_{\max}$ are explained as the wavelength, the lower and upper bounds of the optical sweep, $I_{RT}(\lambda)$ and $I_T(\lambda)$ are explained as the normalized absorption intensities of un-annealed and annealed films, respectively. When the overall absorption intensity changes significantly, it suggests that the inherent properties of the material have undergone a glass transition, and the corresponding temperature is T_g.

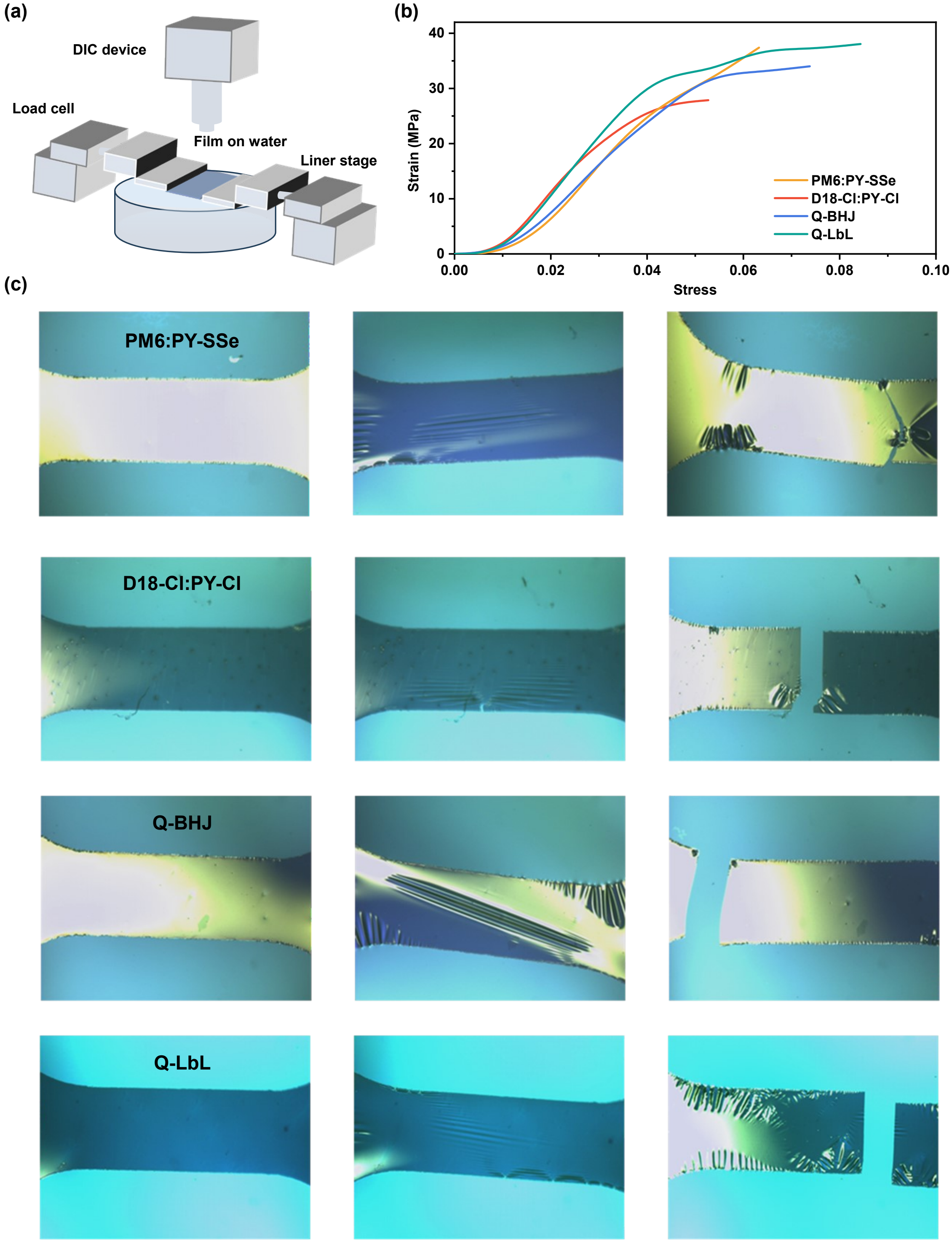

Figure S23. (a) Schematic illustration of the tensile tester setup for floating polymer blend films. b) Stress–strain curves of relevant polymer blend films. (c) Optical microscope images of PM6:PY-SSe, D18-Cl:PY-Cl, Q-BHJ and Q-LbL blend films' morphological change during the tensile test via the film-on-water (FOW) method. The deep-green color represents the water phase while the white-silver color represents our polymer films. From left to right, the change in film morphology under gradually increasing stretching is shown.

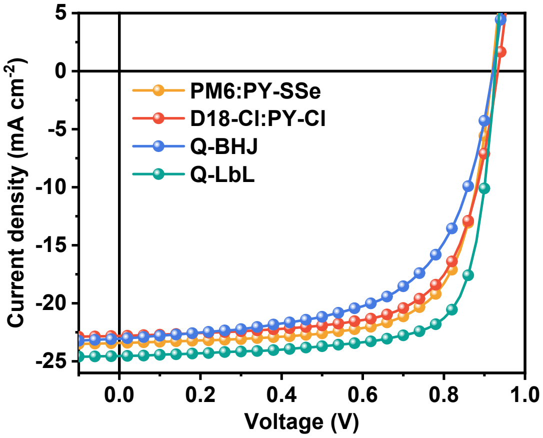

Figure S24. *J–V* characteristics of flexible all-PSCs under simulated AM 1.5G illumination.

Table S10. Summary of photovoltaic parameters of the flexible all-PSCs measured under the illumination of AM 1.5 G at 100 mW cm^{-2}.

Active layer	V_{OC} [V]	J_{SC} [mA cm^{-2}]	FF [%]	PCE[a)] [%]
PM6:PY-SSe	0.920	23.42	70.03	15.09 (14.78±0.10)
D18-Cl:PY-Cl	0.933	22.81	68.15	14.50 (14.22±0.16)
Q-BHJ	0.921	23.04	61.13	12.97 (12.76±0.17)
Q-LbL	0.926	24.55	74.89	17.02 (16.78±0.09)

[a)] The average PCE values with standard deviations were obtained from 10 independent cells.

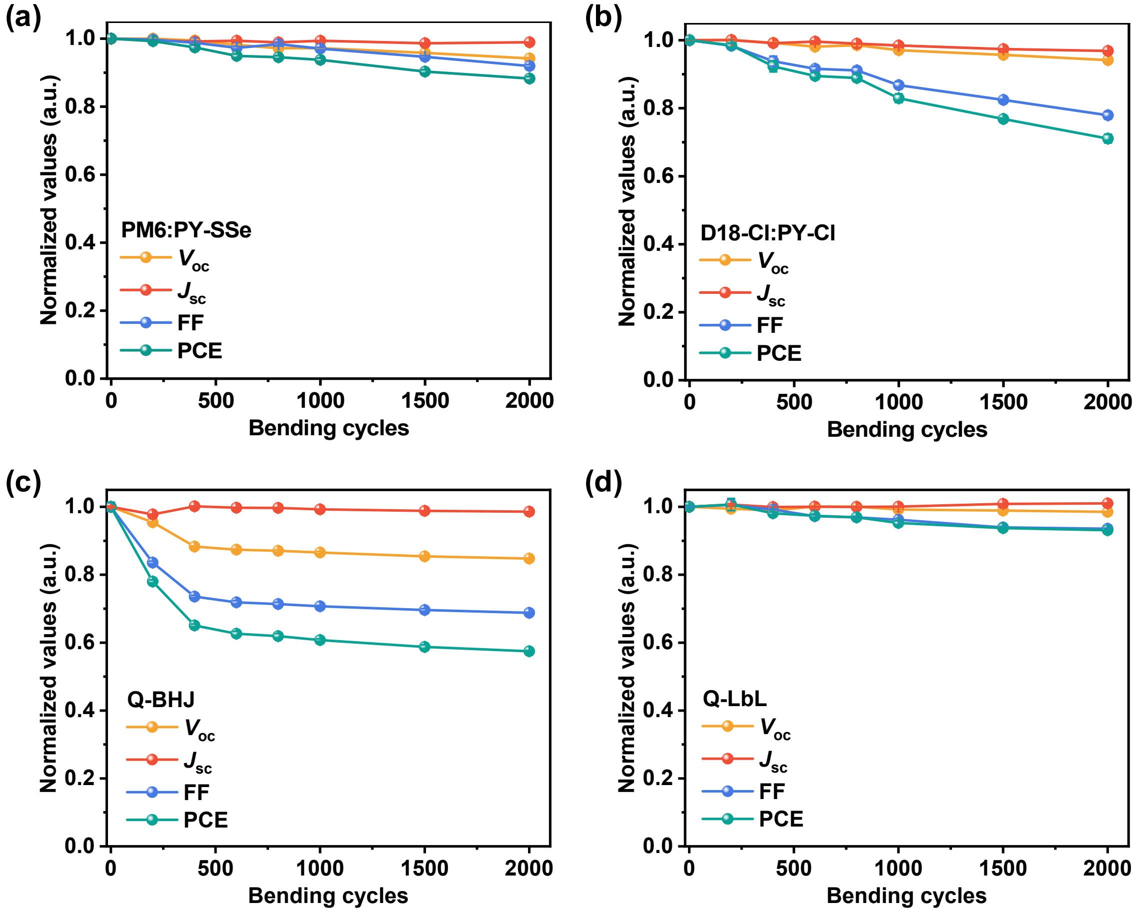

Figure S25. Normalized photovoltaic parameters of relevant flexible all-PSCs (a) PM6:PY-SSe, (b) D18-Cl:PY-Cl, (c) Q-BHJ, (d) Q-LbL) as functions of bending cycles. In each bending cycle, the flexible devices were folded with a bending radius of 2 mm.

Table S11. The exciton generation, charge collection, charge recombination and charge extraction lifetime of the relevant devices.

Active layer	$\eta_{\mathrm{diss}}{}^{a}$ [%]	$\eta_{\mathrm{coll}}{}^{b}$ [%]	G^{c} [$\times10^{28}$ m^{-3} s^{-1}]	α^{d}	n^{e} [kT/q]	$\tau_{\mathrm{TPC}}{}^{f}$ [μs]	$\tau_{\mathrm{TPV}}{}^{g}$ [μs]	$\mu_h/\mu_e{}^{h}$
PM6:PY-SSe	97.65	85.10	1.61	0.986	1.39	0.20	2.67	1.27
D18-Cl:PY-Cl	93.79	74.11	1.58	0.988	1.46	0.23	2.30	0.86
Q-BHJ	91.83	73.86	1.54	0.980	1.74	0.25	1.59	20.6
Q-LbL	97.89	85.59	1.64	0.998	1.24	0.18	2.85	1.01

[a] Under short circuit condition. [b] Under the maximal power output condition. [c] The maximum rate of exciton generation calculated from the relationship of $J_{\mathrm{sat}} = qLG_{\mathrm{max}}$. [d] $J_{sc} \propto P_{in}^{\alpha}$. [e] $V_{oc} \propto (nkT/q)\ln P_{in}$. [f] Charge extraction time extract from TPC. [g] Carrier lifetime extract from TPV. [h] The ratio of electron mobility to hole mobility calculated from SCLC measurements.

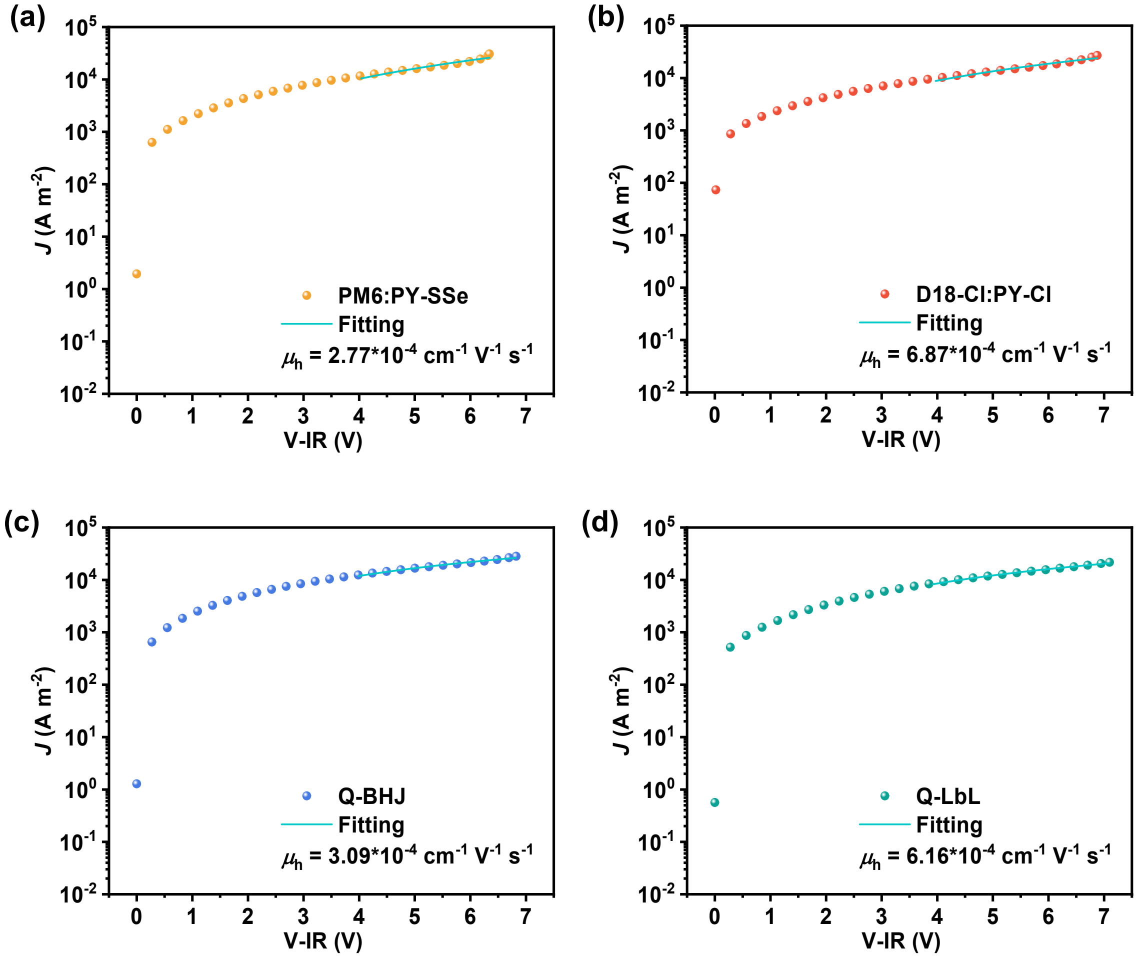

Figure S26. The dark *J-V* characteristics of PM6:PY-SSe, D18-Cl:PY-Cl, Q-BHJ and Q-LbL based hole-only devices. The solid lines represent the best fitting using the SCLC model.

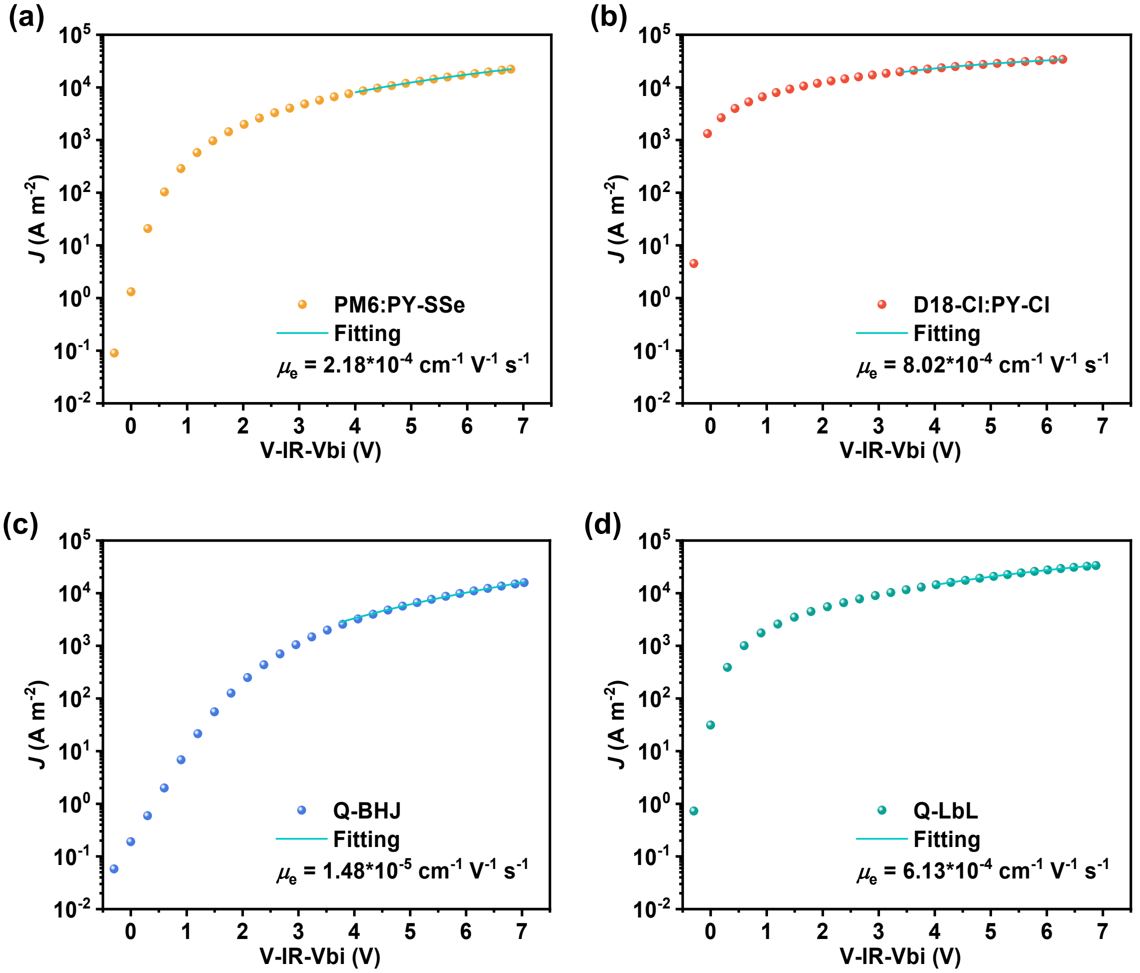

Figure S27. The dark *J-V* characteristics of PM6:PY-SSe, D18-Cl:PY-Cl, Q-BHJ and Q-LbL based electron-only devices. The solid lines represent the best fitting using the SCLC model.

Table S12. Hole and electron mobilities of the pristine and blend films determined from the SCLC measurements for binary and quaternary blends.

Active layer	Thickness [nm]	Hole-only [$\times 10^{-4}$ cm^2 V^{-1} s^{-1}]	Thickness [nm]	Electron-only [$\times 10^{-4}$ cm^2 V^{-1} s^{-1}]
PM6:PY-SSe	82.56	2.77	95.45	2.18
D18-Cl:PY-Cl	90.45	6.87	96.48	8.02
Q-BHJ	88.67	3.09	84.76	0.15
Q-LbL	93.64	6.16	94.78	6.13

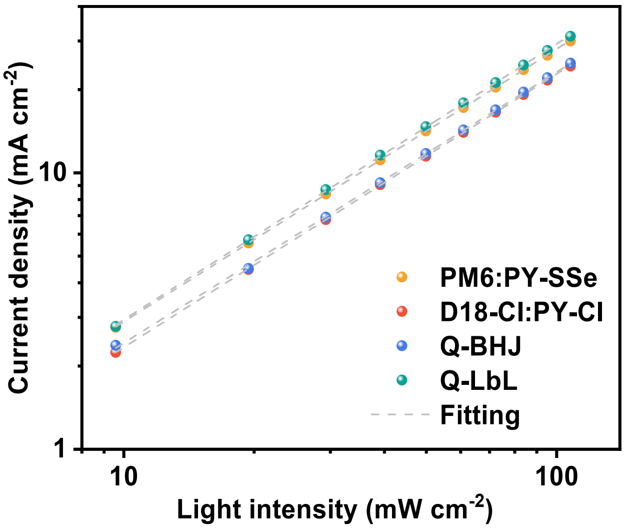

Figure S28. Dependence of J_{SC} on the light intensity of the devices. The dashed lines represent linear fits of the data.

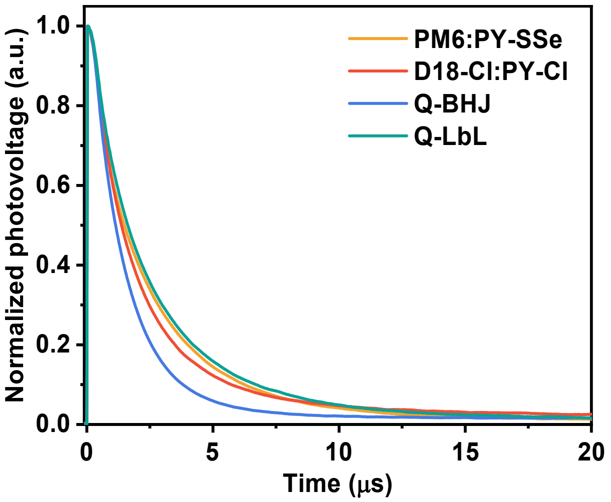

Figure S29. Normalized TPV data of the investigated devices.

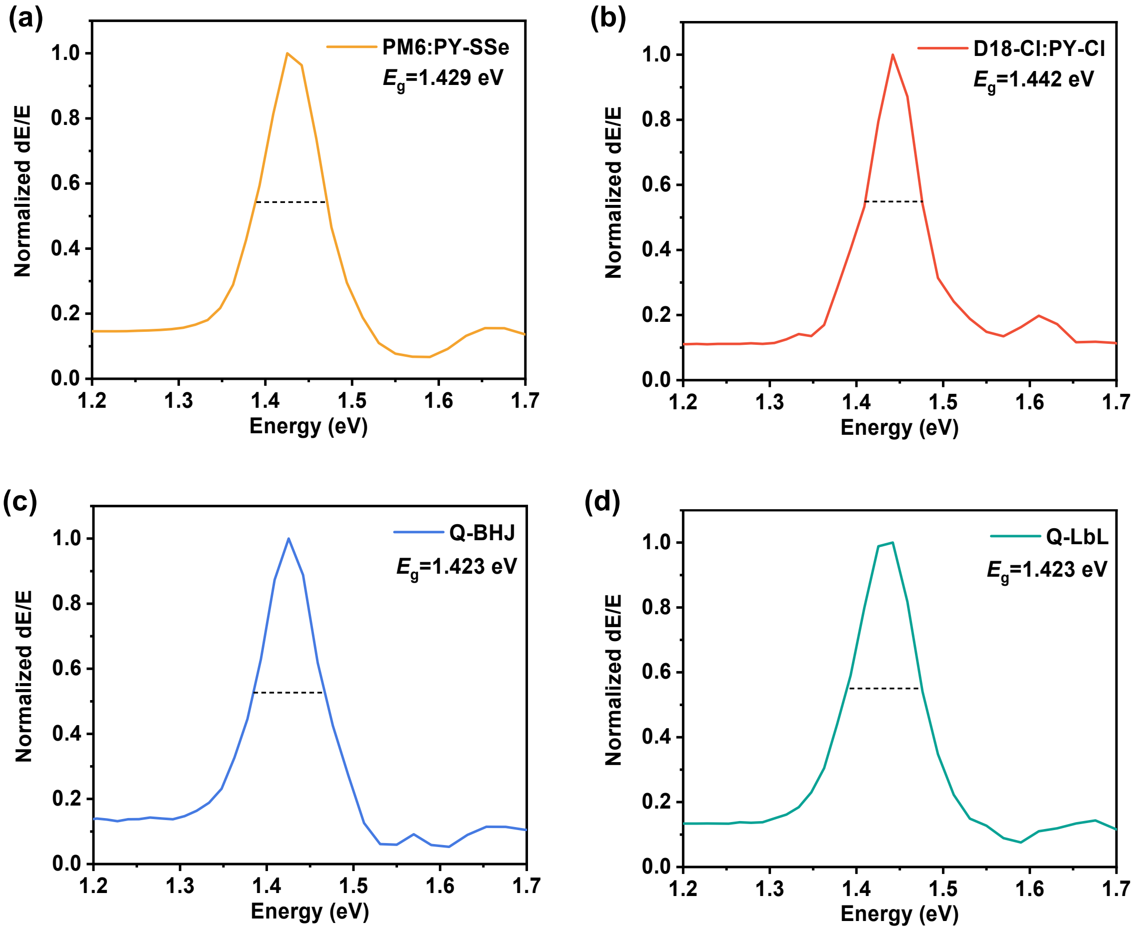

Figure S30. Bandgap of the four investigated all-polymer systems calculated from their the first-order differential of the EQE curves of all-PSC devices based on (a) PM6:PY-SSe, (b) D18-Cl:PY-Cl, (c) Q-BHJ and (d) Q-LbL blends.

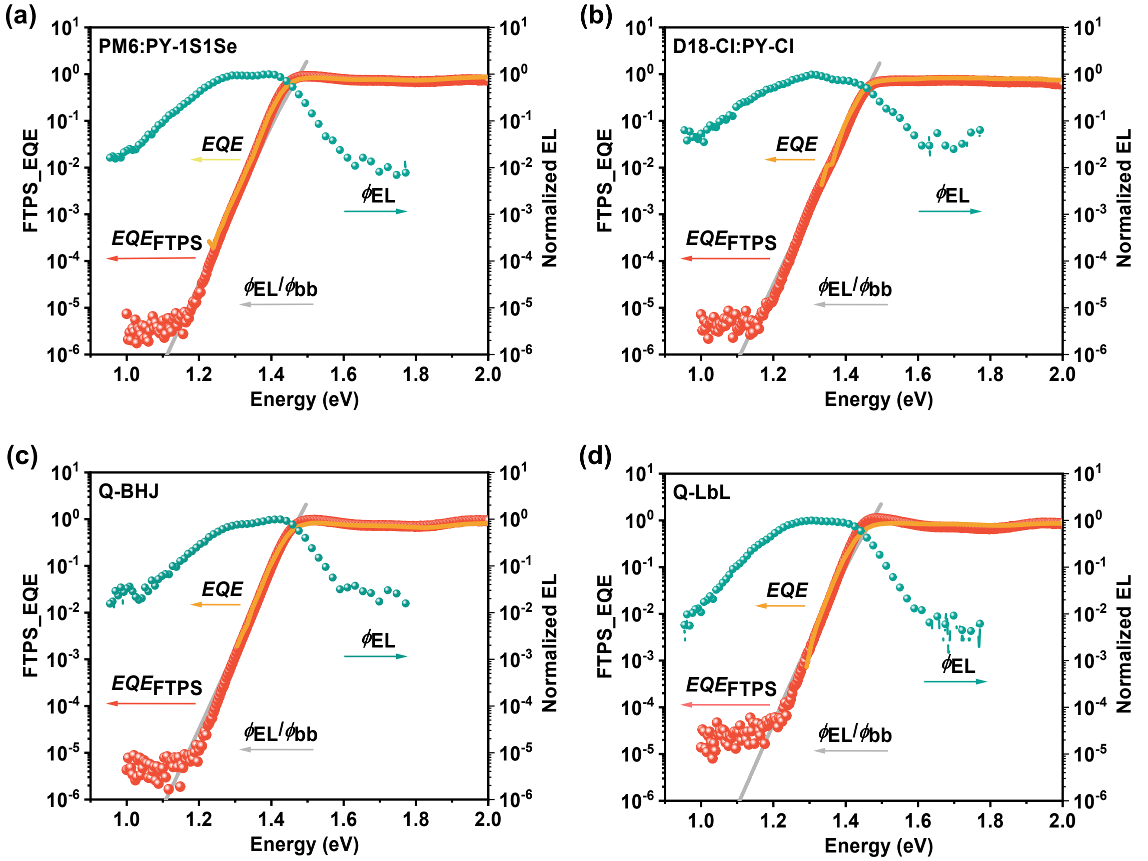

Figure S31. Semi-logarithmic plots of normalized EL, measured EQE and EQE calculated by FTPS (EQE_{FTPS}) as a function of energy for devices based on (a) PM6:PY-SSe, (b) D18-Cl:PY-Cl, (c) Q-BHJ and (d) Q-LbL blends. The ratio of ϕ_{EL}/ϕ_{bb} was used to plot the EQE in the low-energy regime, where ϕ_{EL} and ϕ_{bb} represent the emitted photon flux and the room-temperature blackbody photon flux, respectively.

Table S13. Measured and calculated parameters to quantify the non-radiative recombination losses of the optimized binary and ternary devices.

Device	E_g[a] (eV)	V_{oc}[b] (V)	E_{loss} (eV)	VSQ oc (V)	ΔE_1 (eV)	Vrad oc[c] (V)	ΔE_2 (eV)	ΔE_3 (eV)
PM6:PY-SSe	1.429	0.919	0.510	1.175	0.254	1.118	0.057	0.199
D18-Cl:PY-Cl	1.425	0.937	0.488	1.170	0.255	1.133	0.027	0.196
Q-BHJ	1.427	0.924	0.502	1.173	0.254	1.127	0.046	0.203
Q-LbL	1.423	0.930	0.493	1.168	0.255	1.122	0.046	0.192

[a] E_{gap} was determined from the intersection of the EQE edge and the local EQE maximum. [b] V_{oc} was calculated from the measured J-V curves. [c] Vrad oc was calculated from FTPS and EL measurements.

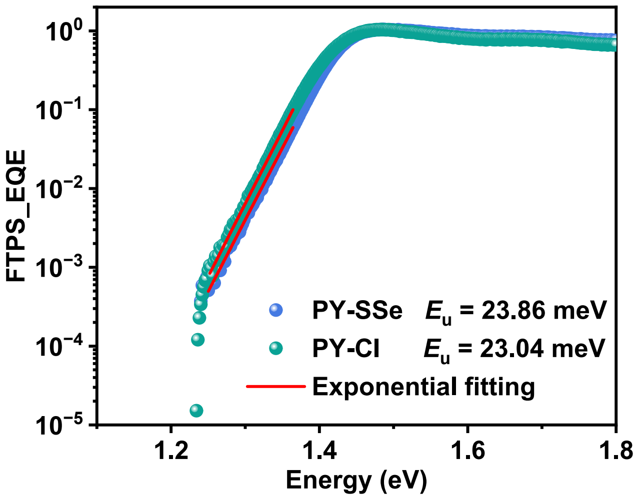

Figure S32. The FTPS-EQE spectra of the pristine PY-SSe and PY-Cl based devices.

Figure S33. Photographs of water and ethylene glycol droplets on the top surfaces of neat (a) PM6, D18-Cl, PY-SSe and PY-Cl films. (b) PM6:PY-SSe, D18-Cl:PY-Cl, Q-BHJ and Q-LbL blend films. The contact angle measurement is conducted at the center of the substrates, avoiding the edges of the ITO anodes to ensure the flatness of the film surfaces.

Table S14. Investigations of the contact angles, surface energy, wetting coefficient and interfacial tension values of PM6, D18-Cl, PY-SSe and PY-Cl.

Material	Contact angle		Surface energy [mJ m^{-2}]	Relative χ	
	Water	Ethylene glycol		(With PM6)	(With D18-Cl)
PM6	103.20	78.20	36.20	/	0.13
D18-Cl	104.20	76.80	40.68	0.13	/
PY-SSe	101.30	71.80	46.93	0.70	0.22
PY-Cl	100.90	73.90	38.70	0.04	0.03
PM6:PY-SSe	102.30	74.70	40.90	/	/
D18-Cl:PY-Cl	104.50	74.20	50.97	/	/
Q-BHJ	103.40	73.90	47.66	/	/
Q-LbL	103.00	74.70	43.38	/	/

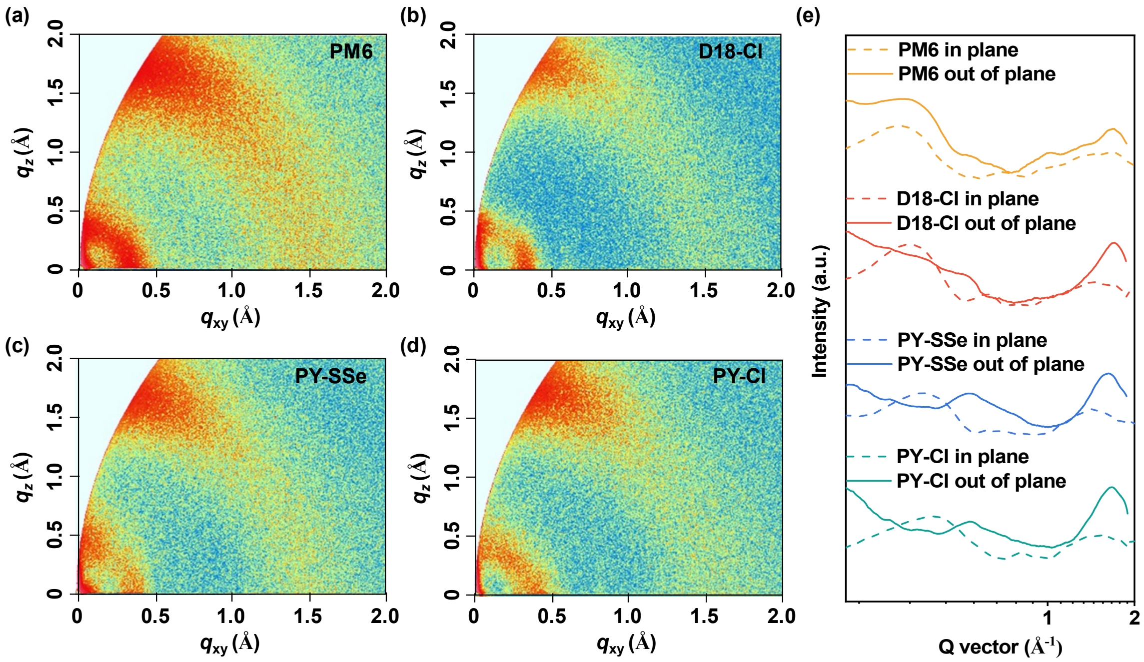

Figure S34. 2D GIWAXS patterns of pristine (a) PM6, (b) D18-Cl, (c) PY-SSe and (d) PY-Cl. (e) IP and OOP extracted line-cut profiles of relevant films.

Table S15. Investigations of the morphology parameters extracted from the GIWAXS measurements of PM6, PY-SSe, D18-Cl and PY-Cl.

Material	In plane				Out of plane			
	Lamellar stacking (100)				π-π stacking (010)			
	q (Å^{-1})	*d* (Å)	FWHM (Å^{-1})	CCL (Å)	*q* (Å^{-1})	*d* (Å)	FWHM (Å^{-1})	CCL (Å)
PM6	0.308	20.38	0.150	41.87	1.701	3.692	0.312	20.13
D18-Cl	0.328	19.15	0.146	43.01	1.697	3.701	0.246	25.53
PY-SSe	0.368	17.07	0.181	34.70	1.628	3.857	0.274	22.92
PY-Cl	0.400	15.70	0.207	30.34	1.667	3.767	0.262	23.97

Table S16. Investigations of the morphology parameters extracted from the GIWAXS measurements of PM6:PY-SSe, D18-Cl:PY-Cl, Q-BHJ and Q-LbL blend films.

Material	In plane				Out of plane			
	Lamellar stacking (100)				π-π stacking (010)			
	q (Å^{-1})	*d* (Å)	FWHM (Å^{-1})	CCL (Å)	*q* (Å^{-1})	*d* (Å)	FWHM (Å^{-1})	CCL (Å)
PM6:PY-SSe	0.325	19.32	0.139	45.18	1.668	3.765	0.275	22.84
D18-Cl:PY-Cl	0.338	18.58	0.137	45.84	1.678	3.743	0.250	25.12
Q-BHJ	0.330	19.03	0.135	46.52	1.678	3.743	0.268	23.43
Q-LbL	0.333	18.86	0.135	46.52	1.665	3.772	0.239	26.28

Reference

[1] L. Zhang, X. Zhu, D. Deng, Z. Wang, Z. Zhang, Y. Li, J. Zhang, K. Lv, L. Liu, X. Zhang, H. Zhou, H. Ade and Z. Wei, *Adv. Mater.*, 2022, **34**, e2106316.

[2] L. Zhan, S. Li, Y. Li, R. Sun, J. Min, Z. Bi, W. Ma, Z. Chen, G. Zhou, H. Zhu, M. Shi, L. Zuo and H. Chen, *Joule*, 2022, **6**, 662-675.

[3] M. Gao, Z. Liang, Y. Geng and L. Ye, Chem. Commun., 2020, **56**, 12463-12478.

[4] Z. G. Zhang, Y. Yang, J. Yao, L. Xue, S. Chen, X. Li, W. Morrison, C. Yang and Y. Li, *Angew. Chem. Int. Ed.*, 2017, **56**, 13503-13507.

[5] H. Yao, F. Bai, H. Hu, L. Arunagiri, J. Zhang, Y. Chen, H. Yu, S. Chen, T. Liu, J. Y. L. Lai, Y. Zou, H. Ade and H. Yan, *ACS Energy Lett.*, 2019, **4**, 417-422.

[6] J. Wu, Y. Meng, X. Guo, L. Zhu, F. Liu and M. Zhang, *J. Mater. Chem. A*, 2019, **7**, 16190-16196.

[7] Q. Fan, W. Su, S. Chen, W. Kim, X. Chen, B. Lee, T. Liu, U. A. Méndez-Romero, R. Ma, T. Yang, W. Zhuang, Y. Li, Y. Li, T.-S. Kim, L. Hou, C. Yang, H. Yan, D. Yu and E. Wang, *Joule*, 2020, **4**, 658-672.

[8] T. Jia, J. Zhang, W. Zhong, Y. Liang, K. Zhang, S. Dong, L. Ying, F. Liu, X. Wang, F. Huang and Y. Cao, *Nano Energy*, 2020, **72**, 104718.

[9] Q. Fan, Q. An, Y. Lin, Y. Xia, Q. Li, M. Zhang, W. Su, W. Peng, C. Zhang, F. Liu, L. Hou, W. Zhu, D. Yu, M. Xiao, E. Moons, F. Zhang, T. D. Anthopoulos, O. Inganäs and E. Wang, *Energy Environ. Sci.*, 2020, **13**, 5017-5027.

[10] W. Wang, Q. Wu, R. Sun, J. Guo, Y. Wu, M. Shi, W. Yang, H. Li and J. Min, *Joule*, 2020, **4**, 1070-1086.

[11] Q. Fan, R. Ma, T. Liu, W. Su, W. Peng, M. Zhang, Z. Wang, X. Wen, Z. Cong, Z. Luo, L. Hou, F. Liu, W. Zhu, D. Yu, H. Yan and E. Wang, *Sol. RRL*, 2020, **4**, 2000142.

[12] J. Du, K. Hu, L. Meng, I. Angunawela, J. Zhang, S. Qin, A. Liebman-Pelaez, C. Zhu, Z. Zhang, H. Ade and Y. Li, *Angew. Chem. Int. Ed*, 2020, **59**, 15181-15185.

[13] L. Zhu, W. Zhong, C. Qiu, B. Lyu, Z. Zhou, M. Zhang, J. Song, J. Xu, J. Wang, J. Ali, W. Feng, Z. Shi, X. Gu, L. Ying, Y. Zhang and F. Liu, *Adv. Mater.*, 2019, **31**, 1902899.

[14] Y. Li, Z. Jia, Q. Zhang, Z. Wu, H. Qin, J. Yang, S. Wen, H. Y. Woo, W. Ma, R. Yang and J. Yuan, *ACS Appl. Mater. Interfaces*, 2020, **12**, 33028-33038.

[15] S. Seo, C. Sun, J. W. Lee, S. Lee, D. Lee, C. Wang, T. N. L. Phan, G. U. Kim, S. Cho, Y. H. Kim and B. J. Kim, *Adv. Funct. Mater*, 2021, **32**, 2108508.

[16] Q. Fan, W. Su, S. Chen, T. Liu, W. Zhuang, R. Ma, X. Wen, Z. Yin, Z. Luo, X. Guo, L. Hou, K. Moth-Poulsen, Y. Li, Z. Zhang, C. Yang, D. Yu, H. Yan, M. Zhang and E. Wang, *Angew. Chem. Int. Ed.*, 2020, **59**, 19835-19840.

[17] H. Sun, H. Yu, Y. Shi, J. Yu, Z. Peng, X. Zhang, B. Liu, J. Wang, R. Singh, J. Lee, Y. Li, Z. Wei, Q. Liao, Z. Kan, L. Ye, H. Yan, F. Gao and X. Guo, *Adv. Mater.*, 2020, **32**, 2004183.

[18] Y. Wu, Q. Wu, W. Wang, R. Sun and J. Min, *Sol. RRL*, 2020, **4**, 2000409.

[19] F. Peng, K. An, W. Zhong, Z. Li, L. Ying, N. Li, Z. Huang, C. Zhu, B. Fan, F. Huang and Y. Cao, *ACS Energy Lett.*, 2020, **5**, 3702-3707.

[20] C. Zhu, Z. Li, W. Zhong, F. Peng, Z. Zeng, L. Ying, F. Huang and Y. Cao, *Chem. Commun.*, 2021, **57**, 935-938.

[21] J. W. Lee, C. Sun, B. S. Ma, H. J. Kim, C. Wang, J. M. Ryu, C. Lim, T. S. Kim, Y. H. Kim, S. K. Kwon and B. J. Kim, *Adv. Energy Mater.*, 2020, **11**, 202003367.

[22] L. Zhang, T. Jia, L. Pan, B. Wu, Z. Wang, K. Gao, F. Liu, C. Duan, F. Huang and Y. Cao, *Sci. China Chem.*, 2021, **64**, 408-412.

[23] N. Su, R. Ma, G. Li, T. Liu, L.-W. Feng, C. Lin, J. Chen, J. Song, Y. Xiao, J. Qu, X. Lu, V. K. Sangwan, M. C. Hersam, H. Yan, A. Facchetti and T. J. Marks, *ACS Energy Lett.*, 2021, **6**, 728-738.

[24] Q. Wu, W. Wang, Y. Wu, Z. Chen, J. Guo, R. Sun, J. Guo, Y. Yang and J. Min, *Adv. Funct. Mater*, 2021, **31**, 2010411.

[25] S. Huang, P. Cong, Z. Liu, F. Wu, C. Gong, L. Chen and Y. Chen, *Sol. RRL*, 2021, **5**, 2100019.

[26] H. Yu, M. Pan, R. Sun, I. Agunawela, J. Zhang, Y. Li, Z. Qi, H. Han, X. Zou, W. Zhou, S. Chen, J. Y. L. Lai, S. Luo, Z. Luo, D. Zhao, X. Lu, H. Ade, F. Huang, J. Min and H. Yan, *Angew. Chem. Int. Ed.*, 2021, **60**, 10137-10146.

[27] H. Wang, H. Chen, W. Xie, H. Lai, T. Zhao, Y. Zhu, L. Chen, C. Ke, N. Zheng and F. He, *Adv. Funct. Mater*, 2021, **31**, 2100877.

[28] F. Wu, J. Liu, J. Liu, J. Oh, B. Huang, D. Chen, Z. Liu, Q. He, C. Yang and L. Chen, *ChemElectroChem*, 2021, **8**, 3936-3942.

[29] H. Fu, Y. Li, J. Yu, Z. Wu, Q. Fan, F. Lin, H. Y. Woo, F. Gao, Z. Zhu and A. K. Y. Jen, *J. Am. Chem. Soc*, 2021, **143**, 2665-2670.

[30] H. Yu, S. Luo, R. Sun, I. Angunawela, Z. Qi, Z. Peng, W. Zhou, H. Han, R. Wei, M. Pan, A. M. H. Cheung, D. Zhao, J. Zhang, H. Ade, J. Min and H. Yan, *Adv. Funct. Mater*, 2021, **31**, 2100791.

[31] Q. Wu, W. Wang, Y. Wu, R. Sun, J. Guo, M. Shi and J. Min, *Natl. Sci. Rev.*, 2022, **9**, nwab151.

[32] J. Du, K. Hu, J. Zhang, L. Meng, J. Yue, I. Angunawela, H. Yan, S. Qin, X. Kong, Z. Zhang, B. Guan, H. Ade and Y. Li, *Nat. Commun.*, 2021, **12**, 5264.

[33] L. Zhou, X. Xia, L. Meng, J. Zhang, X. Lu and Y. Li, *Chem. Mater.*, 2021, **33**, 8212-8222.

[34] Q. Fan, H. Fu, Z. Luo, J. Oh, B. Fan, F. Lin, C. Yang and A. K. Y. Jen, *Nano Energy*, 2022, **92**, 106718.

[35] Z. Genene, J. W. Lee, S. W. Lee, Q. Chen, Z. Tan, B. A. Abdulahi, D. Yu, T. S. Kim, B. J. Kim and E. Wang, *Adv. Mater.*, 2021, **34**, 2107361.

[36] H. Fu, Q. Fan, W. Gao, J. Oh, Y. Li, F. Lin, F. Qi, C. Yang, T. J. Marks and A. K. Y. Jen, *Sci. China Chem.*, 2021, **65**, 309-317.

[37] T. Zhao, C. Cao, H. Wang, X. Shen, H. Lai, Y. Zhu, H. Chen, L. Han, T. Rehman and F. He, *Macromolecules*, 2021, **54**, 11468-11477.

[38] H. Yu, Y. Wang, H. K. Kim, X. Wu, Y. Li, Z. Yao, M. Pan, X. Zou, J. Zhang, S. Chen, D. Zhao, F. Huang, X. Lu, Z. Zhu and H. Yan, *Adv. Mater.*, 2022, **34**, 2200361.

[39] C. Cao, H. Wang, D. Qiu, T. Zhao, Y. Zhu, X. Lai, M. Pu, Y. Li, H. Li, H. Chen and F. He, *Adv. Funct. Mater*, 2022, **32**, 2201828.

[40] G. Sun, X. Jiang, X. Li, L. Meng, J. Zhang, S. Qin, X. Kong, J. Li, J. Xin, W. Ma and Y. Li, *Nat. Commun.*, 2022, **13**, 5267.

[41] M. Deng, X. Xu, W. Qiu, Y. Duan, R. Li, L. Yu and Q. Peng, *Angew. Chem. Int. Ed.*, 2024, **63**, 202405243.

[42] Y. Pan, L. Guo, M. H. Jee, G. Dai, Z. Ge, J. Zhang, X. Duan, J. Song, X. Li, H. Y. Woo and Y. Sun, *Adv. Energy Mater.*, 2024, DOI: 10.1002/aenm.202403747.

[43] Z. Luo, T. Liu, R. Ma, Y. Xiao, L. Zhan, G. Zhang, H. Sun, F. Ni, G. Chai, J. Wang, C. Zhong, Y. Zou, X. Guo, X. Lu, H. Chen, H. Yan and C. Yang, *Adv. Mater.*, 2020, **32**, 2005942.

[44] Y. Zhu, H. Guo, X. Xiong, D. Cai, Y. Ma and Q. Zheng, *Adv. Mater.*, 2024, **36**, 2314169.

[45] H. Xiao, J. Lv, M. Liu, X. Guo, X. Xia, X. Lu and M. Zhang, *J. Mater. Chem. A*, 2023, **11**, 5584-5592.

[46] X. Yang, R. Sun, Y. Wang, M. Chen, X. Xia, X. Lu, G. Lu and J. Min, *Adv. Mater.*, 2022, **35**, 2209350.

[47] X. Wu, X. Yang, Y. Shao, Y. Gao, J. Wan, S. Ponomarenko, Y. Luponosov, R. Sun and J. Min, *Sol. RRL*, 2023, **7**, 2300064.

[48] Y. Li, J. Song, Y. Dong, H. Jin, J. Xin, S. Wang, Y. Cai, L. Jiang, W. Ma, Z. Tang and Y. Sun, *Adv. Mater.*, 2022, **34**, 2110155.

[49] Y. Diao, Y. Zhou, T. Kurosawa, L. Shaw, C. Wang, S. Park, Y. Guo, J. A. Reinspach, K. Gu, X. Gu, B. C. Tee, C. Pang, H. Yan, D. Zhao, M. F. Toney, S. C. Mannsfeld and Z. Bao, *Nat. Commun.*, 2015, **6**, 7955.

[50] X. Gu, Y. Zhou, K. Gu, T. Kurosawa, Y. Guo, Y. Li, H. Lin, B. C. Schroeder, H. Yan, F. Molina-Lopez, C. J. Tassone, C. Wang, S. C. B. Mannsfeld, H. Yan, D. Zhao, M. F. Toney and Z. Bao, *Adv. Energy Mater.*, 2017, **7**, 1602742.

[51] W. Zhao, S. Zhang, Y. Zhang, S. Li, X. Liu, C. He, Z. Zheng and J. Hou, *Adv. Mater.*, 2018, **30**, 1704837.

[52] H. Hu, L. Ye, M. Ghasemi, N. Balar, J. J. Rech, S. J. Stuard, W. You, B. T. O'Connor and H. Ade, *Adv. Mater.*, 2019, **31**, 1808279.

[53] L. Zhu, W. Zhong, C. Qiu, B. Lyu, Z. Zhou, M. Zhang, J. Song, J. Xu, J. Wang, J. Ali, W. Feng, Z. Shi, X. Gu, L. Ying, Y. Zhang and F. Liu, *Adv. Mater.*, 2019, **31**, 1902899.

[54] Y. Lin, L. Yu, Y. Xia, Y. Firdaus, S. Dong, C. Müller, O. Inganäs, F. Huang, T. D. Anthopoulos, F. Zhang and L. Hou, *Sol. RRL*, 2019, **3**, 1900179.

[55] L. Zhang, H. Zhao, J. Yuan, B. Lin, Z. Xing, X. Meng, L. Ke, X. Hu, W. Ma and Y. Yuan, *Org. Electron.*, 2020, **82**, 105725.

[56] S. A. Schneider, K. L. Gu, H. Yan, M. Abdelsamie, Z. Bao and M. F. Toney, *Chem. Mater.*, 2021, **33**, 5951-5961.

[57] Q. Wu, W. Wang, Y. Wu, Z. Chen, J. Guo, R. Sun, J. Guo, Y. Yang and J. Min, *Adv. Funct. Mater.*, 2021, **31**, 2010411.

[58] Y. Zhang, N. Wang, Y. Wang, J. Zhang, J. Liu and L. Wang, *iScience*, 2021, **24**, 103104.

[59] H. Yu, M. Pan, R. Sun, I. Agunawela, J. Zhang, Y. Li, Z. Qi, H. Han, X. Zou, W. Zhou, S. Chen, J. Y. L. Lai, S. Luo, Z. Luo, D. Zhao, X. Lu, H. Ade, F. Huang, J. Min and H. Yan, *Angew. Chem. Int. Ed.*, 2021, **60**, 10137-10146.

[60] D. Chen, S. Liu, B. Huang, J. Oh, F. Wu, J. Liu, C. Yang, L. Chen and Y. Chen, *Small*, 2022, **18**, 2200734.

[61] D. Chen, S. Liu, X. Hu, F. Wu, J. Liu, K. Zhou, L. Ye, L. Chen and Y. Chen, *Sci. China Chem.*, 2021, **65**, 182-189.

[62] Y.-Z. Zhang, N. Wang, Y.-H. Wang, J.-H. Miao, J. Liu and L.-X. Wang, *Chinese J. Polym. Sci.*, 2022, **40**, 989-995.

[63] J. Liu, J. Liu, J. Deng, B. Huang, J. Oh, L. Zhao, L. Liu, C. Yang, D. Chen, F. Wu and L. Chen, *J. Energy Chem.*, 2022, **71**, 631-638.

[64] Y. Yue, B. Zheng, W. Yang, L. Huo, J. Wang and L. Jiang, *Adv. Mater.*, 2022, **34**, 2108508.

[65] A. Harillo-Baños, Q. Fan, S. Riera-Galindo, E. Wang, O. Inganäs and M. Campoy-Quiles, *ChemSusChem*, 2022, **15**, e202101888.

[66] N. Yao, Q. Fan, Z. Genene, H. Liu, Y. Xia, G. Wen, Y. Yuan, E. Moons, J. van Stam, W. Zhang, X. Lu, E. Wang and F. Zhang, *Sol. RRL*, 2023, **7**, 2201134.

[67] Y. Qin, N. Balar, Z. Peng, A. Gadisa, I. Angunawela, A. Bagui, S. Kashani, J. Hou and H. Ade, *Joule*, 2021, **5**, 2129-2147.

[68] M. Ghasemi, N. Balar, Z. Peng, H. Hu, Y. Qin, T. Kim, J. J. Rech, M. Bidwell, W. Mask, I. McCulloch, W. You, A. Amassian, C. Risko, B. T. O'Connor and H. Ade, *Nat. Mater.*, 2021, **20**, 525-532.